Acta Materialia 303 (2026) 121696

Contents lists available at ScienceDirect

Acta Materialia

journal homepage: www.elsevier.com/locate/actamat

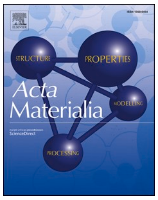

Effect of nanoscale cellular structure on the mechanical properties of Inconel 718 with unique hierarchical structure fabricated by laser powder bed fusion

Ken Cho [a,b], Kippei Yamashita [a], Shinnosuke Kakutani [a], Takuma Saito [c], Taisuke Sasaki [c], Katsuhiko Sawaizumi [a], Masayuki Okugawa [a,b], Yuichiro Koizumi [a,b], Tsuyoshi Mayama [d], Taichi Kikukawa [a], Ozkan Gokcekaya [a,b], Takuya Ishimoto [a,e], Hajime Kimizuka [f], Wu Gong [g], Takuro Kawasaki [g], Stefanus Harjo [g], Takayoshi Nakano [a,b], Hiroyuki Y. Yasuda [a,b,*]

[a] *Division of Materials and Manufacturing Science, Graduate School of Engineering, The University of Osaka, 2-1 Yamadaoka, Suita, Osaka 565-0871, Japan*
[b] *Anisotropic Design & Additive Manufacturing Research Center, Graduate School of Engineering, The University of Osaka, 2-1 Yamadaoka, Suita, Osaka 565-0871, Japan*
[c] *Research Center for Magnetic and Spintronic Materials, National Institute for Materials Science, 1-2-1, Sengen, Tsukuba, Ibaraki 305-0047, Japan*
[d] *Department of Materials Science and Engineering, Kumamoto University, 2-39-1, Kurokami, Chuo-ku, Kumamoto 860-8555, Japan*
[e] *Aluminium Research Center, University of Toyama, 3190 Gofuku, Toyama 930-8555, Japan*
[f] *Department of Materials Design Innovation Engineering, Graduate School of Engineering, Nagoya University, Furo-cho, Chikusa-ku, Nagoya, Aichi, 464-8603, Japan*
[g] *J-PARC Center, Japan Atomic Energy Agency, 2-4 Shirakata, Tokai-mura, Naka-gun, Ibaraki, 319-1195, Japan*

ARTICLE INFO

Keywords:
Additive manufacturing
Nickel superalloys
Crystallographic texture
Cellular structure
Strengthening mechanism
Neutron diffraction

ABSTRACT

The deformation behavior and strengthening mechanism of Inconel 718 with a hierarchical structure composed of microscale crystallographic lamellar microstructure (CLM) and nanoscale cellular structure, fabricated by laser powder bed fusion, were clarified via nanoscale microstructural and *in-situ* neutron diffraction analyses. The CLM is a layered structure parallel to the building direction (BD) and consists of relatively wide main and narrow sub-layers with $\langle 110 \rangle$ and $\langle 100 \rangle$ orientations, respectively, with respect to BD. This is the first study to demonstrate that the yield stress of the alloys depends strongly on deformation stresses of the sub-layers, even though Schmid factors of the primary slip system for both layers are the same. The sub-layer continues to deform elastically even beyond the micro-yield point of the main layer, which results in the macroscopic strengthening at an early stage of deformation. On the other hand, the cellular structure is formed in both layers, associated with a dendritic cell growth along $\langle 100 \rangle$ direction, Nb segregation between the cells and an accumulation of dislocations to decrease a residual stress. The cell boundaries with numerous dislocations and Nb segregation act as a strong barrier to dislocation motion resulting in a stress increase through the Hall-Petch law, even though they are low-angle grain boundaries. The spacing and morphology of the cell boundary depend strongly on fabrication conditions. The optimized cellular structure provides significant strengthening comparable to or greater than that caused by large-angle grain boundaries, thereby increasing the macroscopic strength of the alloys through hardening of the sub-layer.

1. Introduction

Ni-based superalloys are widely used in high-temperature environments such as aerospace and power generation facilities because of their excellent high-temperature strength and oxidation resistance [1–4]. In recent years, further strengthening of Ni-based superalloys is desired for realizing higher efficiency in aircraft engines and power generation systems. Many practical Ni-based superalloys such as Inconel 718 alloys

---

* Corresponding author at: Division of Materials and Manufacturing Science, Graduate School of Engineering, The University of Osaka, 2-1 Yamadaoka, Suita, Osaka 565-0871, Japan.
E-mail address: hyyasuda@mat.eng.osaka-u.ac.jp (H.Y. Yasuda).

https://doi.org/10.1016/j.actamat.2025.121696
Received 21 May 2025; Received in revised form 6 October 2025; Accepted 1 November 2025

are precipitation-strengthened alloys, wherein the γ' ($L1_2$ structure: $Ni_3(Al, Ti)$) and γ '' ($D0_{22}$ structure: Ni_3Nb) phases are precipitated coherently in the γ phase (face-centered cubic (fcc) structure). Consequently, the researches and developments of various new alloys focusing on the morphology of the γ' and γ'' phases are being actively carried out [5–8]. Meanwhile, innovations have also been made in manufacturing processes for Ni-based superalloy products in recent years. In particular, researches on metal additive manufacturing (AM) technique which is a new fabrication process for metal products are being vigorously pursued [9,10].

The typical AM process of powder bed fusion (PBF) for metallic materials has attracted considerable attention for metal products, particularly for applications in the aerospace, energy and biomedical industries, where a high degree of complexity is required [11–14]. In the PBF process, metallic parts with complex shapes and internal structures can be manufactured directly by melting and layering metal powder layers with a focused laser or electron beam based on three-dimensional (3D) computer-aided design data. In addition to Ni-based superalloys, extensive studies have been made on the use of the PBF process for manufacturing various structural materials such as Ti alloys [15,16], Fe alloys [17,18], Al alloys [19,20], intermetallic materials [21–26] and high entropy alloys [27–29], focusing on improving dimensional accuracy and reducing defects. Moreover, the relationship between the microstructure and mechanical properties of the alloys has also been investigated. The results reveal that PBF alloys prepared under specific process conditions exhibit unique microstructures and excellent mechanical properties, compared to those of conventionally cast or forged alloys [30–34]. Ishimoto et al. reported that a significant reduction in Young's modulus can be achieved by imparting a single-crystalline microstructure to β-type Ti alloys using the laser PBF (L-PBF) process [35]. Further, Todai et al. developed an electron beam PBF process for TiAl alloys to obtain a unique layered microstructure that consists of two regions with completely different microstructural morphologies, and they succeeded in improving the room temperature (RT) ductility of the alloys [36]. The formation of these unique microstructures can be attributed to the important features of the PBF process, such as dynamic temperature variations in and near the melt pool and repeated thermal effect from the melt pool [37,38]. Thus, the PBF process is accredited as a novel metal part manufacturing process that is useful and effective for controlling not only the shape but also the microstructure and mechanical and/or functional properties of the metal parts [39,40].

More recently, Gokcekaya et al. revealed that Inconel 718 alloys which have a unique lamellar structure with a width of several tens of micrometers, parallel to BD, can be obtained using the L-PBF process under appropriate process parameters and scan strategy [41]. The conventional lamellar structure is multilayered microstructure with different crystalline structures, such as the ferrite (α) / cementite phases for Fe alloys and the bcc (β) / hcp (α) phases for Ti alloys. However, the newly discovered lamellar structure in Inconel 718 alloys formed after the L-PBF process is composed of two layers with the same crystal structure (the γ phase) but different crystallographic orientations. Thus, this layered structure is referred to as a crystallographic lamellar microstructure (CLM) [41]. The relatively wide main layer and narrow sub-layer are oriented in the $\langle 110 \rangle$ and $\langle 100 \rangle$ orientations, respectively, with respect to BD. In addition, each layer has a columnar cellular structure with an average spacing of several hundred nanometers. Similar nanoscale cellular structures have been observed in polycrystalline Fe and Cu alloys prepared by L-PBF [42–44]. The cellular structure consists of the columnar dislocation cells of which boundaries are accompanied by segregation of certain elements. It was also found that the Inconel 718 rods with the hierarchical structure composed of the CLM and nanoscale cells show excellent mechanical properties and large strength anisotropy [41,45]. The ultimate tensile strength of the alloys in BD is higher than 1000 MPa, even without precipitation of the γ' and γ'' phases. Undoubtedly, this remarkable increase in strength is accompanied by the unique hierarchical microstructure. Thus, the mechanical properties of Ni-based superalloy components are expected to be significantly improved by controlling the morphology of the hierarchical structure through the optimization of the L-PBF fabrication process. However, the effects of the process conditions such as the laser power (P) or input energy density (ED) on these microstructures, especially the formation mechanism and morphology of nanoscale cellular structure, are still unclear. In addition, although several previous studies suggested that the cellular structure improves the strength of the alloys [42–44], the effects of the CLM and the cellular structure on strength, including the deformation behavior of each layer and influence of their morphologies, have not yet been clarified in detail.

In the present study, the characteristics of the CLM and cellular structure formed in the Inconel 718 alloys fabricated by L-BPF were investigated by electron microscopy analyses at various scales and quantitative elemental analysis by 3D atom probe (3DAP) tomography techniques. Moreover, the deformation behaviors of the main and sub-layers in the CLM were investigated via *in-situ* neutron diffraction (ND) technique and numerical simulation using the crystal plasticity finite element method (FEM). The effects of the microstructure on the mechanical properties of the alloys were also examined, focusing on the morphology of the cellular structure.

2. Experimental

2.1. Sample fabrication by L-PBF

Inconel 718 powder with an average particle diameter of approximately 30 μm produced by Ar gas atomization was used as a raw material in the present study. The chemical composition of the raw powders is listed in Table 1. Rectangular rods with dimensions of 10 × 10 × 30 mm (short rod, Fig. 1(a)) and 10 × 10 × 60 mm (long rod, Fig. 1(b)) were fabricated using the EOS M290 L-PBF system. The layer thickness (h) for each fed powder layer was 60 μm and BD was parallel to the longitudinal direction of the rods. To obtain the CLM, the process parameters and scanning strategy were determined according to our previous study [41]. A Yb-fiber laser was scanned bidirectionally in the x-direction (scan direction, SD) for every layer at a scan speed (v) of 1000 mm/s and a hatch spacing (d) of 80 μm. Six process conditions with different P (240–360 W) were used for the fabrication of the rods. The values of ED for these conditions were calculated to be between 50.0–75.0 J/mm^3 according to Eq. (1).

$$ED = \frac{P}{vhd} \tag{1}$$

Three types of the rods prepared with minimum, medium and maximum P values (P = 240, 300 and 360 W, respectively) were selected for the detailed microstructural analyses and deformation behavior investigations. The values of ED for the fabrication conditions with the minimum, medium and maximum P are 50.0, 62.5 and 75.0 J/mm^3, respectively. Hereafter, the three types of the rods are referred to as low (ED = 50.0 J/mm^3), middle (62.5 J/mm^3) and high ED (75.0 J/mm^3) rods. In addition, to understand the effect of the cellular structure on the mechanical properties, some high ED rods were heat treated at 1373 K for 1 h to remove the cellular structure (hereafter, referred to as HT sample).

2.2. Microstructural characterization

The microstructure was observed via a scanning electron microscope (SEM) equipped with an electron backscattered diffraction (EBSD) detector, a transmission electron microscope (TEM), a scanning TEM (STEM) and 3DAP tomography. The TEM and STEM observations were performed at accelerating voltages of 300 kV and 200 kV, respectively. 3DAP analyses were performed in voltage pulse mode with a pulse fraction of 20 % at a base temperature of 30 K. The acquired 3DAP

Table 1
Chemical composition of Inconel 718 raw powder (wt. %).

	Ni	Cr	Nb	Mo	Ti	Al	Co	Cu	Si	Mn	Fe
Raw powder	51.4	19.8	5.5	3.2	1.1	0.55	0.01	0.10	0.04	0.01	Bal.

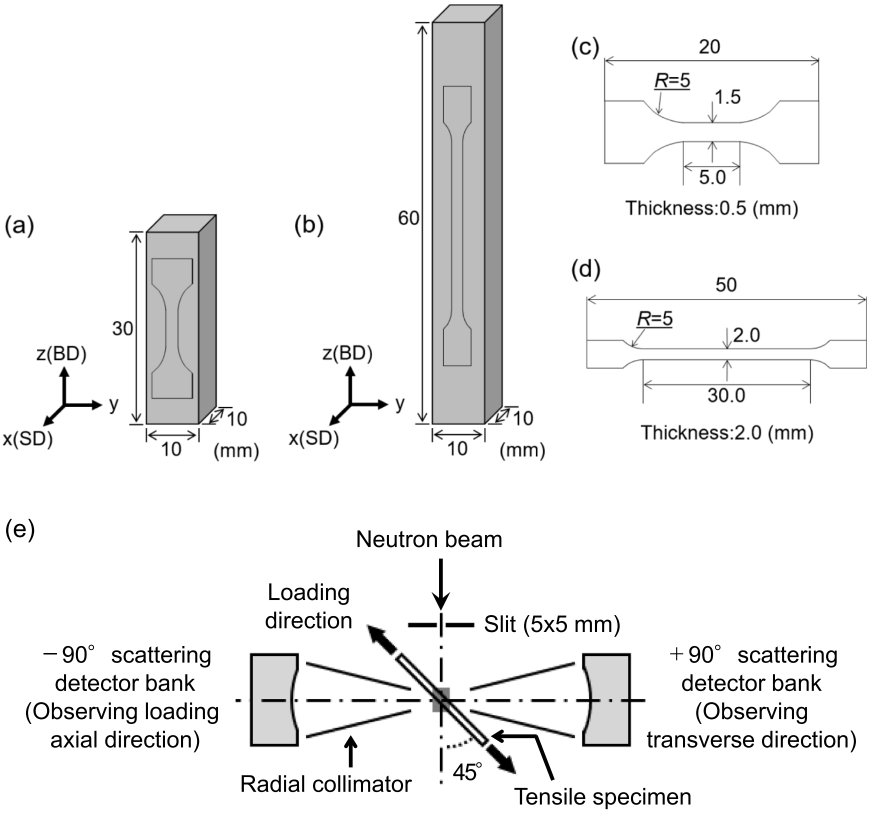

Fig. 1. Schematic drawings of the short (a) and long (b) rods fabricated by L-PBF and specimen configurations for the tensile tests (c) and *in-situ* ND analyses (d). (e) Schematic drawing of the setup for the *in-situ* ND analyses.

datasets were analyzed using IVAS 3.8.16 software. Specimens for STEM and 3DAP analyses were fabricated by a standard lift-out method using dual-beam focused ion beam (FIB)/SEM system.

2.3. Mechanical testing

The tensile properties of the rods fabricated by L-PBF at the six different *ED* were evaluated using an Instron-type testing machine at RT in air with an initial strain rate of 1.7 × 10^{-4} s^{-1}. The specimens for the tensile tests with gauge dimensions of 5.0 × 1.5 × 0.5 mm were cut from the center of the short rods using electro-discharge machining (Fig. 1(c)). The loading axis was set parallel to the longitudinal direction of the rods (in other words, parallel to BD). In addition, the influence of the morphology of the nanoscale cellular structure on the hardness of each layer of the CLM was investigated using nanoindentation tests at y-z cross section with a maximum load of 19.6 mN. The specimens for these mechanical tests were polished mechanically using both waterproof emery papers and colloidal SiO_2 suspensions.

2.4. Deformation behavior analysis

To understand the elastic and plastic deformation behaviors of the main and sub-layers of the CLM, *in-situ* ND measurements under tensile loading were performed using a time-of-flight engineering diffractometer TAKUMI (BL19) at the Materials and Life Science Experimental Facility of the Japan Proton Accelerator Research Complex (J-PARC). The tensile specimens with gauge dimensions of 30.0 × 2.0 × 2.0 mm (Fig. 1(d)) were pulled at RT in air with an initial strain rate of 1.7 × 10^{-4} s^{-1} using a tensile loading machine placed on the sample stage of TAKUMI. The specimens for the *in-situ* ND analyses were cut from the center of the long rods by electro-discharge machining and polished to a mirror surface using the same method as those used for the tensile tests. They were mounted horizontally on a loading machine and inclined at 45° with respect to the incident direction of the neutron beam. The ND patterns for the loading axial and transversal directions were measured using two detector banks with 5 mm collimators and scattering angles of ±90°, as illustrated in Fig. 1(e). Note that the ND patterns for the loading axial direction were analyzed in this study. Details of the measurement setups are well described in ref [46,47]. Diffraction patterns were extracted at a constant time interval (10 s) corresponding to a nominal strain increment of 0.17 % until the strain reached 4.6 % to investigate variations in the lattice strain of the main and sub-layers during deformation. The lattice strain related to the {*hkl*} diffraction plane (ε_{hkl}) was calculated by

$$\varepsilon_{hkl} = \frac{d_{hkl} - d_{hkl}^{0}}{d_{hkl}^{0}} \tag{2}$$

where d_{hkl}^{0} and d_{hkl} represent the lattice spacings of the {*hkl*} plane in the stress-free and stress-loaded states, respectively. The ND patterns were analyzed by single-peak analysis using the Z-Rietveld software [48] to evaluate d_{hkl}^{0} and d_{hkl}. The diffraction peaks attributed to the (220) or

(200) planes were used to investigate ε_{hkl} of the main or sub-layers, respectively.

In addition, the crystal plasticity FEM was employed to understand the development of ε_{hkl} of both main and sub-layers during deformation evaluated by the *in-situ* ND analyses. The numerical analysis was performed using a static explicit large deformation FEM with a rate-dependent crystal plasticity constitutive model [49]. A finite element mesh used in this study was identical to the model used in the previous study [45] where main and sub-layers are explicitly modelled as similar to actual lamellar structure with crystal orientations for each layer (Fig. S1). The {111}<110> slip system which is the primary slip system in fcc metals was implemented in the calculation model. The detailed calculation method and material parameters employed in this numerical analysis are described in the previous paper [45] and supplementary note (Tables S1 and S2).

2.5. Numerical simulation of solidification behavior

In order to discuss the formation mechanism of the cellular structure, solidification conditions such as the temperature gradient (G) and cooling rate (CR) of the melt pool were analyzed numerically based on computational thermal-fluid dynamics (CtFD). The CtFD simulations of a laser-beam irradiated on Inconel 718 were performed using a 3D thermo-fluid analysis software (Flow Science. FLOW-3D® with Flow-3D Weld module [50]). In this numerical analysis, a Gaussian heat source model, wherein the irradiation intensity distribution of the beam has a Gaussian distribution over the entire beam, was used as the heat source. The intensity distribution ($\dot{q}(r_{\mathrm{e}})$) of the laser beam at a beam radius (r_{a}) is expressed as

$$\dot{q}(r_{\mathrm{e}}) = \frac{2\eta P}{\pi r_{\mathrm{e}}^2}\exp\left(-\frac{2r_{\mathrm{a}}^2}{r_{\mathrm{e}}^2}\right) \tag{3}$$

where η and r_{e} represent the beam absorption rate of Inconel 718 and effective beam radius (88 μm), respectively. η was calculated assuming multiple reflections using the Fresnel equation with a Fresnel coefficient of 0.135. A high vapor pressure is generated at the melt pool surface because of the evaporation of the alloy. This vapor pressure acts as a recoil pressure (P_{recoil}) on the surface, which pushes the melt pool down. P_{recoil} can be reproduced using

$$P_{\mathrm{recoil}} = AP_0\exp\left[\frac{\Delta H_{\mathrm{LV}}}{R_{\mathrm{c}}T_{\mathrm{V}}}\left(1-\frac{T_{\mathrm{V}}}{T}\right)\right] \tag{4}$$

where A, P_0, ΔH_{LV}, R_{c}, T_{V} and T represent the ratio of the recoil pressure caused by evaporation to the vapor pressure on the liquid surface in the equilibrium state, atmospheric pressure (1 atm), latent heat of vaporization, gas constant, vaporization temperature and absolute temperature, respectively. The parameters required for the simulation are listed in Table 2. In this study, the value of A was assumed to be 0.54, the same as in the previous studies [37]. The emissivity (e) and Stefan–Boltzmann constant ($\sigma_{\mathrm{S\text{-}B}}$) were taken from previous study [51], while the average values calculated from the molar ratios and the pure metal values [52] were used as ΔH_{LV} and T_{V}. However, most parameters listed in Table 2 were evaluated using alloy property calculation software (Sente software. JMatPro v12 [53]). The computational domain (6.0 mm in SD, 0.8 mm in width and 0.3 mm in BD) consists of a uniform mesh (10 × 10 × 10 μm) throughout the domain. Continuous boundary conditions were applied to all boundaries except for the top surface. The value of T was initially set to 353 K. This calculation focused on the solidification behavior in the melt pool formed during the second beam scan of the two consecutive beam scans to consider the thermal effects of adjacent beam scans. The scanning conditions of the laser beam, v and d, were fixed at their experimental values of 1000 mm/s and 80 μm, respectively. In contrast, P was varied according to the experimental values and set to 240, 300 and 360 W.

Table 2

Parameters used in the CtFD simulations.

Parameter	Symbol	Value	Ref.
Density at 298.15 K	ρ	8.230 g/cm^3	[*]
Liquidus temperature	T_{L}	1622 K	[*]
Solidus temperature	T_{S}	1382 K	[*]
Viscosity at T_{L}	μ	0.0929 g/cm/s	[*]
Specific heat at 300 K	G_{P}	4.0392 × 10^6 erg/g/K	[*]
Thermal conductivity at 298.15 K	λ_{TC}	1.116 × 10^6 erg/cm/s/K	[*]
Surface tension at T_{L}	γ_{L}	1792 g/s^2	[*]
Temperature coefficient of surface tension	$\mathrm{d}\gamma_{\mathrm{L}}/\mathrm{d}T$	−0.287 J/m^2/K	[*]
Emissivity	E	0.27	[51]
Stefan–Boltzmann constant	$\sigma_{\mathrm{S\text{-}B}}$	5.67 × 10^6 W/m^2/K^4	[51]
Heat of fusion	ΔH_{SL}	2.31 × 10^9 erg/cm/s/K	[*]
Latent heat of vaporization	ΔH_{LV}	6.46 × 10^{10} erg/cm/s/K	[52]
Vaporization temperature	T_{V}	3218 K	[52]

[*] Calculated using JMatPro v12.

3. Results

3.1. The hierarchical microstructure of the Inconel 718 rods fabricated by L-PBF

3.1.1. Effect of ED on the morphology of the hierarchical microstructure

Fig. 2(a)–(c) show x, y and z projections of the EBSD-inverse pole figure (IPF) maps of low (a), middle (b) and high ED (c) rods taken in the y-z cross-section. All rods have the CLM consisting of the <110>//BD-oriented main layers alternating with the <100>//BD-oriented sub-layers. Furthermore, the ⟨100⟩ and ⟨110⟩ directions of the main and sub-layers were parallel to SD (x-direction), respectively. These results mean that both layers are oriented in the ⟨110⟩ direction with respect to the y-direction according to the crystallographic relationships. It should be noted that the average widths of the main and sub-layers in these rods are approximately 55 μm and 25 μm, respectively, regardless of *ED*. Fig. 2(d)–(f) show the typical SEM-backscattered electron (BSE) images of the y-z cross-section of the rods. The white lines in the images indicate the melt pool boundaries. The sub-layer is located at the center of the melt pool, with the main layers on either side. As investigated in detail in previous studies, preferential solidification to the ⟨100⟩ orientation is one of the most important factors in the formation of the crystallographic texture in the L-PBF process [41,54]. Furthermore, the shape of the melt pool, particularly the flatness (radius of curvature) of the bottom, contributes to the formation of the main and sub-layers with different crystallographic orientations [41,54]. The flat geometry of the melt pool bottom delivers stable heat flow and solid/liquid interface migration along BD at the bottom of the melt pool, which results in the formation of the <100>//BD-oriented sub-layer at the center of the melt pool. On the other hand, the main layer is formed by the migration of the solid/liquid interface at 45° to BD on both sides of the melt pool.

As shown in Fig. 2(d)–(f), a fine cellular structure with a white contrast can be seen in both the main and sub-layers of all rods. It should be noted that there are significant differences in the orientation of the cellular structure in each layer. That in the main layer is oriented at 45° to BD (Fig. 2(g)), whereas that in the sub-layer is parallel to BD (Fig. 2(h)). The orientation of the cellular structure is parallel to the solidification direction of each layer, which suggests that the cell formation is closely related to the solidification of the melt pool. It should be also noted that the cell spacing (λ) differs markedly between the main and sub-layers. Fig. 2(i) shows the *ED* dependences of average λ at the central areas of the main and sub-layers (e.g., indicated by yellow circles in Fig. 2(e)). λ of the sub-layer in each rod is narrower than that of the main layer regardless of *ED* based on the Student's *t*-test ($p_{\mathrm{S}} < 0.001$). While there is no noticeable difference in λ of the main layers with different *ED* according to the Tukey's honestly significant difference (HSD) test ($p_{\mathrm{T}} >$

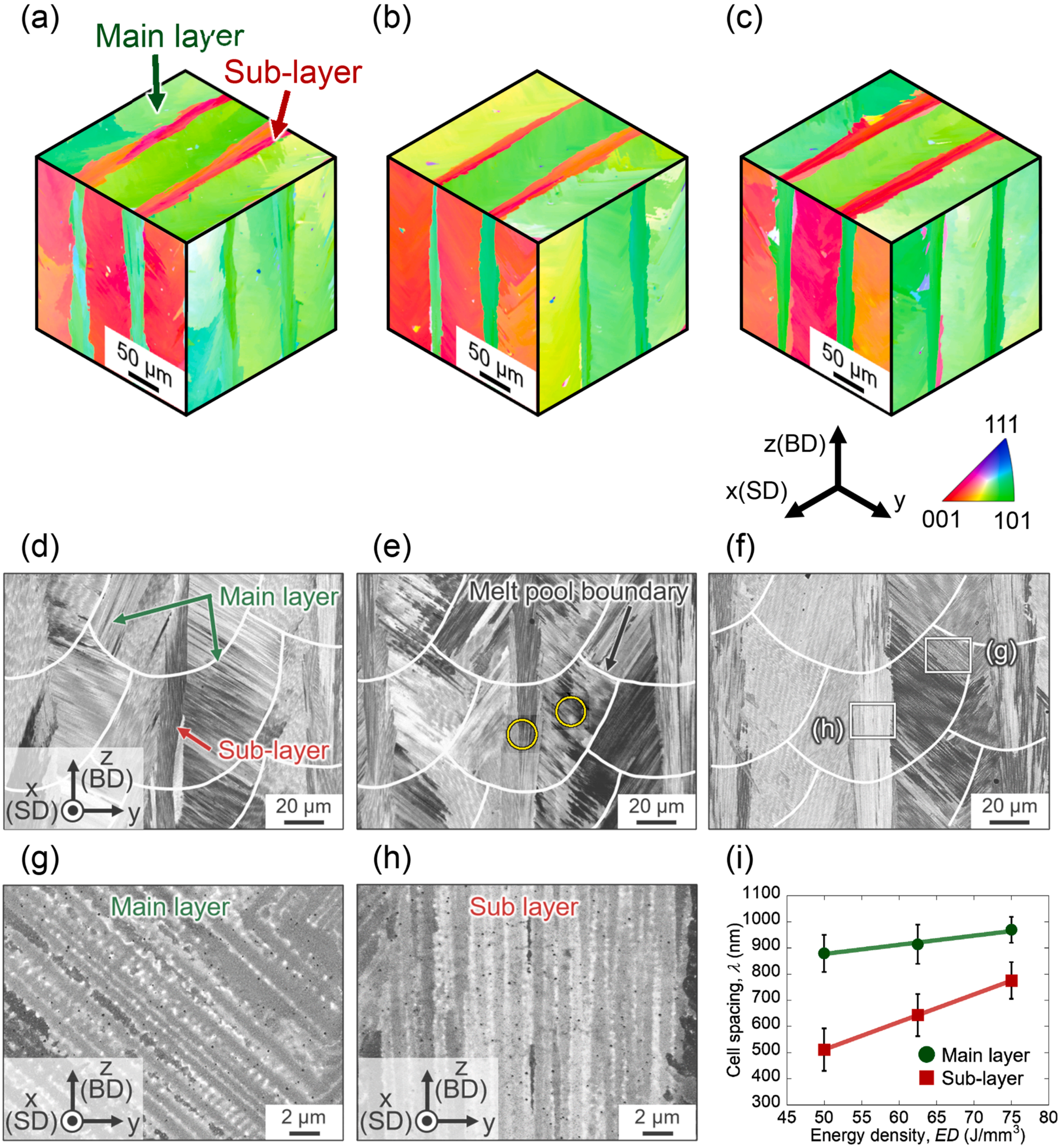

Fig. 2. Typical x, y and z projections of EBSD-IPF maps (a)–(c) and SEM-BSE images (d)–(f) taken in the y-z cross-section of low (a), (d), middle (b), (e) and high (c), (f) ED rods. Enlarged SEM-BSE images of the main (g) and sub-layers (h) in high ED rod. (i) Variations in average λ at the central areas of the main and sub-layers as a function of *ED*.

0.05), λ of the sub-layers decreases significantly from approximately 780 nm to 510 nm with decreasing *ED* ($p_T < 0.001$).

3.1.2. Characterization of the cellular structure

The cellular structure of low ED rod was further analyzed by TEM. Typical TEM-bright field (BF) images of the sub-layer taken from SD and BD are shown in Fig. 3(a) and (b), respectively. The dislocations are tangled to form a dislocation cell, and the columnar dislocation cells with a high density of dislocations are aligned parallel to BD. The spacing between the dislocation cells (400–600 nm) is in good agreement with λ given by SEM-BSE observation in Fig. 2. The dislocation density of the cell interior region is lower than that of the dislocation cell boundary region. However, by TEM analysis, the dislocation density of the cell interior is evaluated to be approximately 3.0×10^{14} m^{-2}, which is equivalent to that of the 10 % cold-rolled Ni-based superalloys [55]. The selected area electron diffraction (SAED) patterns obtained from areas labeled as (c)–(e) in Fig. 3(b) are shown in Fig. 3(c)–(e), respectively. Note that the beam direction was adjusted to [001] in area (c) when obtaining these SAED patterns. The absence of superlattice spots attributed to the γ' and γ'' phases in these SAED patterns indicates that these phases are not precipitated in the as built rods. It should be noted that the beam direction at (d) and (e) slightly deviates from [001]

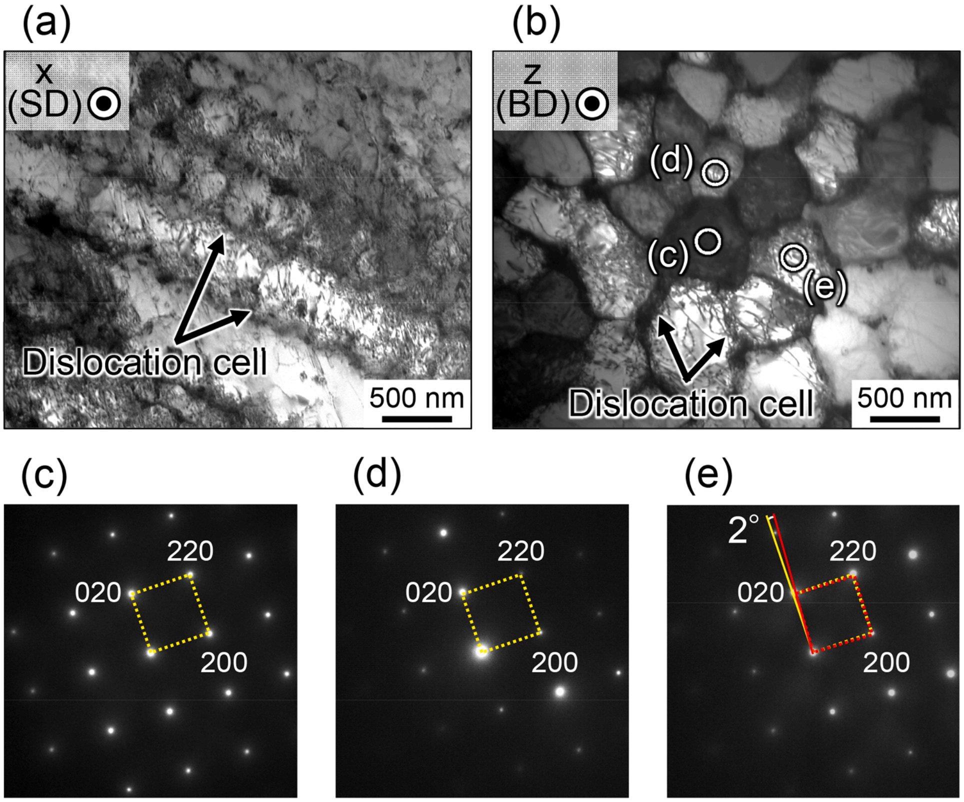

Fig. 3. Typical TEM-BF images of the sub-layer in low ED rod taken from SD (a) and BD (b). (c)–(e) SAED patterns obtained from the areas indicated in (b).

direction. For instance, the beam direction at (e) is rotated by approximately 2° with respect to that at (c). These results suggest that the cell boundary is a low-angle grain boundary (LAGB) with tilt and/or twist components of several degrees.

Fig. 4 shows STEM-high-angle annular dark field (HAADF) image (a) and STEM-energy dispersive spectroscopy (EDS) elemental maps (b)–(j) obtained from the sub-layer of low ED rod, visualizing the elemental partitioning in the cell boundary region with a width of approximately 60 nm and the cell interior region. Nb, Mo and Ti are enriched and Ni, Cr and Fe are depleted in the cell boundary region. Further, fine particles enriched in Nb, Ti, Al, C or O can be seen in the cell boundary region, suggesting the presence of metal carbides (MC) (white arrow), a Laves phase (yellow arrow) and an oxide of aluminum (red arrow) [56,57]. However, the volume fractions of these precipitates are very low and their effects on the mechanical properties seem to be negligible. The 3D atom map of Nb and C for the specimen containing the MC precipitate within the cell boundary region is shown in Fig. 5(a). Note that the MC particle ensures that the cell boundary was included within the 3DAP specimen. The 1D compositional profiles analyzed along the white arrow in Fig. 5(a) are provided as Fig. 5(b) and (c). Nb, Mo and Ti are enriched in the cell boundary region, while Cr and Fe are depleted, which is consistent with the STEM-EDS elemental maps presented in Fig. 4. As summarized in Table 3, the average Nb content in the cell boundary region is approximately 6.4 at %, more than three times higher than that in the cell interior region (approximately 1.8 at %). Furthermore, Ti and Mo are segregated in the cell boundary region at approximately 2.0 at % and 1.9 at %, respectively, and they are twice as much as those inside the cell (Ti: approximately 1.0 at %, Mo: approximately 1.2 at %). In contrast, Cr and Fe concentrations are approximately 20.1 at % and 15.3 at %, respectively, in the cell boundary region, which are lower than those inside the cells (Cr: approximately 22.8 at %, Fe: approximately 20.1 at %). This cellular segregation of specific elements and the small misorientation of several degrees between neighboring cells are consistent with typical features of the dendritic structure formed during solidification. Therefore, the cellular structure is considered to be essentially the same as the dendritic structure without secondary arms. However, the distinct difference from typical dendritic solidification is the development of columnar dislocation cells at the cell boundary region. Therefore, the morphology of the dislocation cell and the relationship between the dislocation cell and segregation region were investigated in detail using STEM analyses.

STEM-HAADF images of the central areas in the sub-layers taken from BD reveal the different morphology of dislocation cells between low and high ED rods (Fig. 6(a) and (b)). Note that the bright contrast in the STEM-HAADF images refers to the diffraction contrast indicating the presence of dislocations, as the Z-contrast difference is negligibly small in the images obtained from these particular samples. As shown in Fig. 6 (a), line-like narrow dislocation cells with a width of only a few tens of nanometers can be observed in low ED rod. In contrast, dislocation cells with a width of several hundreds of nanometers are formed in high ED rod (Fig. 6(b)). Not only the morphology of the dislocation cell, but also the morphology of the segregation region differs between low and high ED rods. Nb concentration maps of the areas marked by white squares in Fig. 6(a) and (b) are shown in Fig. 6(c) and (d), respectively. The width of the segregation region of low ED rods is approximately 60 nm, while that of high ED rods is much wider, spreading to approximately 100 nm. Fig. 6(e) and (f) show enlarged STEM-HAADF images of cell boundaries with narrow (in low ED rod) and wide (in high ED rod) dislocation cells, respectively, and the contrast intensity profiles of the STEM-HAADF images and Nb concentration profiles analyzed by STEM-EDX along the white arrows crossing the cell boundaries. Note that the high contrast intensity of the HAADF images suggests that dislocation is present in the area. It should be noted that the narrow dislocation wall is located at both edges of the segregation region (cell boundary) where the Nb concentration reaches approximately 5.5 at %, while there are few dislocations inside the region, as shown in Fig. 6(e). This result suggests that the narrow dislocation wall is formed by accumulation of the dislocation at the interface between the segregation and cell interior

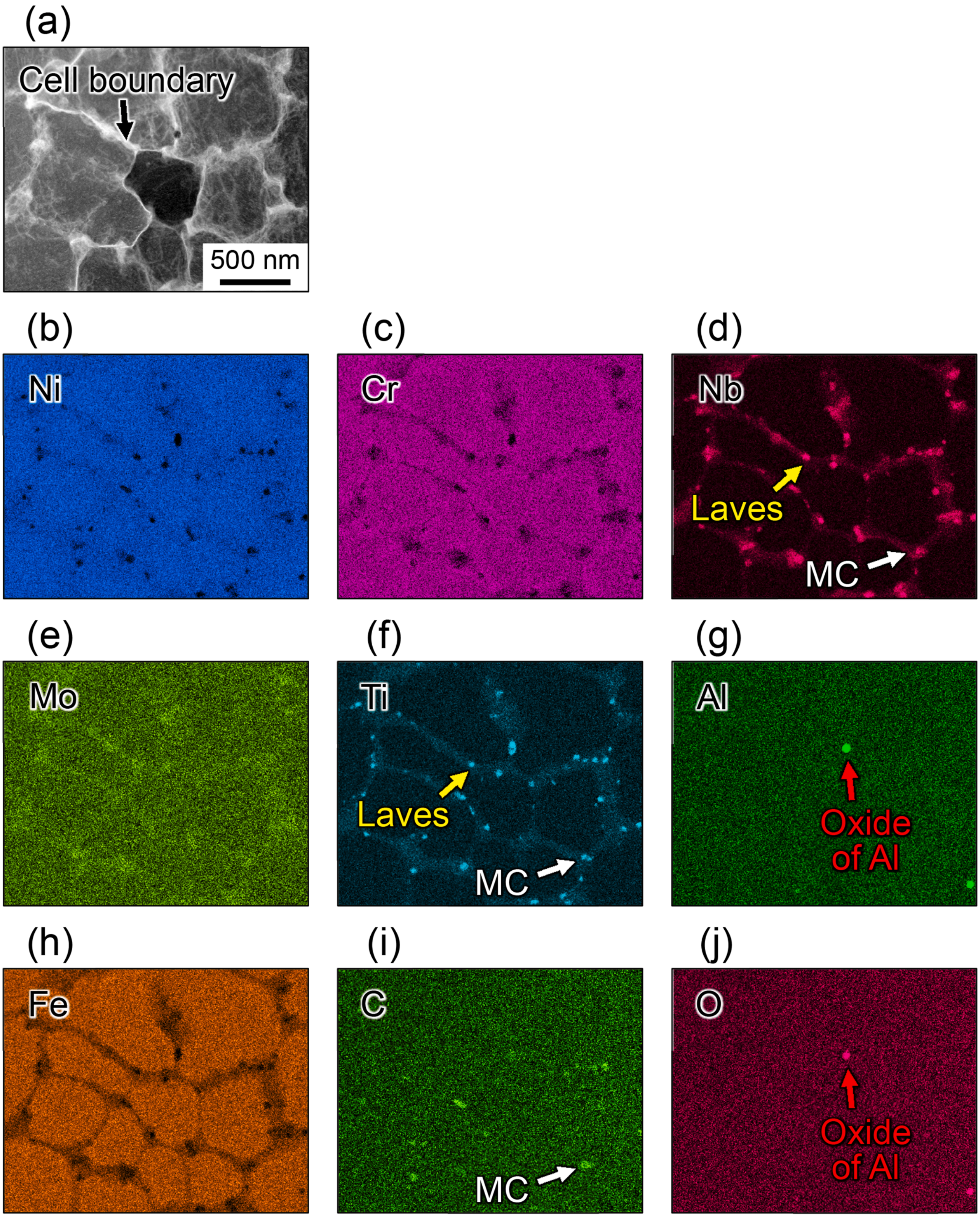

Fig. 4. Typical STEM-HAADF image (a) and elemental maps (b)–(j) of the sub-layer in low ED rod taken from BD using STEM-EDS. (b) Ni, (c) Cr, (d) Nb, (e) Mo, (f) Ti, (g) Al, (h) Fe, (i) C and (j) O.

regions. In contrast, the wide dislocation cell completely overlaps the spread segregation region with a relatively low Nb concentration (approximately 4.0 at %) (Fig. 6(f)). According to these differences in the morphologies of the dislocation cell and segregation region such as Nb content, the cell boundaries can be divided into two types: type I and II as follows:

Type I: a narrow dislocation cell wall (a few tens of nanometers) at both edges of the high Nb segregation region (approximately 5.5 at %) (Fig. 6(e)),

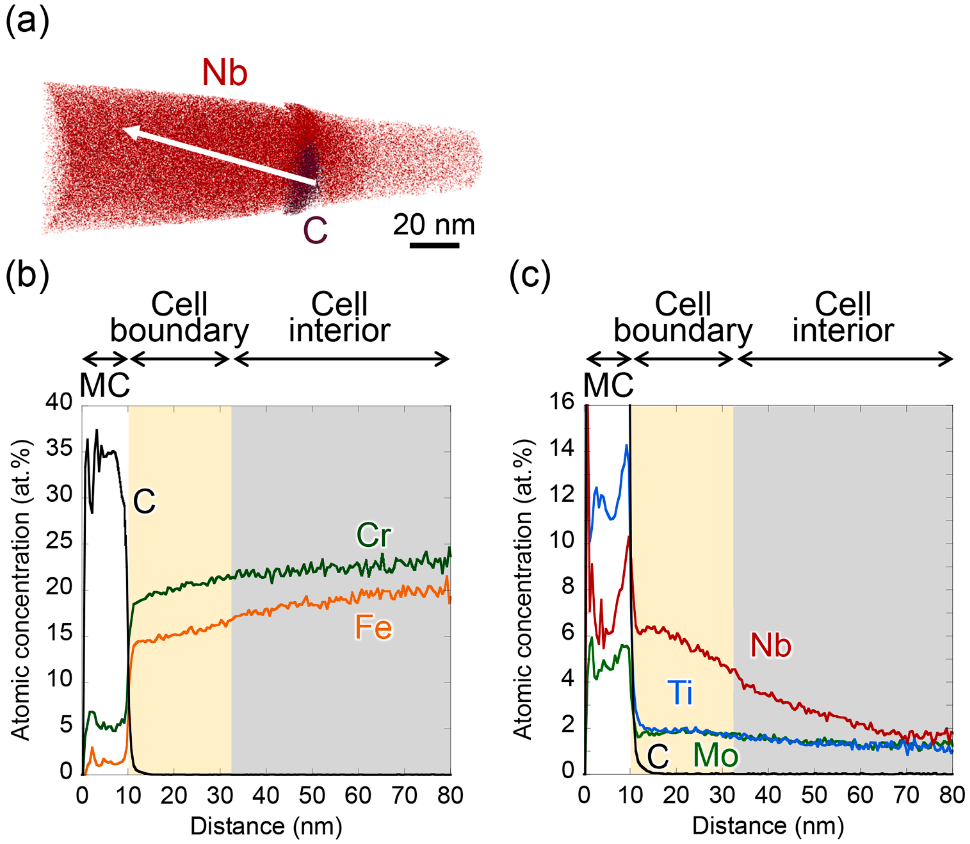

Fig. 5. 3D atom map of Nb and C for the low ED specimen containing MC precipitate within the cell boundary region (a) and 1D compositional profiles of Cr, Fe and C (b) and Nb, Ti, Mo and C (c) along the white arrow indicated in (a).

Table 3
Average compositions of alloying elements at cell boundary and interior of low ED rod evaluated by 3DAP analyses and $k_{I/B}$ of each element. k_0 of each element in the γ matrix calculated by Thermo-calc [62] are also shown in the table.

	Nb	Ti	Mo	Cr	Fe
Cell boundary (at. %)	6.4	2.0	1.9	20.1	15.3
Cell interior (at. %)	1.8	1.0	1.2	22.8	20.1
$k_{I/B}$	0.3	0.5	0.6	1.1	1.3
k_0	0.20	0.42	0.63	1.07	1.18

Type II: a wide dislocation cell wall (several hundreds of nanometers) in the low Nb segregation region (approximately 4.0 at %) (Fig. 6(f)).

It should be noted that the type II is peculiar feature in high ED rod, whereas type I was observed in middle and low ED rods, indicating that a relatively high *ED* is a prerequisite for the development of the type II cell boundary.

3.2. Mechanical properties of Inconel 718 rods with the hierarchical microstructure

3.2.1. Macroscopic strength of the rods

The tensile strength of Inconel 718 rods which have the unique hierarchical microstructure was examined at RT. Fig. 7 shows the yield stresses ($\sigma_{0.2}$) of the rods fabricated under different *ED* conditions. $\sigma_{0.2}$ of the rods increases from approximately 539 MPa to 572 MPa with decreasing *ED*, although these rods have a similar microstructure (i.e., CLM) on the microscopic scale. Further, all rods exhibit a considerably higher strength than HT specimen (approximately 423 MPa) where the nanoscale segregation and dislocation cell wall comprising the cellular structure were eliminated by the heat treatment while maintaining the CLM (Fig. S2). These results indicate that the cellular structure significantly contributes to the strengthening of the alloys.

3.2.2. Deformation behavior of the main and sub-layers

The variations in lattice strain of the main layer (ε_{220}) and sub-layer (ε_{200}) of low, middle and high ED rods during tensile loading were measured via *in-situ* ND analyses to clarify the deformation behavior of each layer of the CLM. The ND patterns of each rod taken from BD before tensile deformation are shown in Fig. 8(a). The diffraction peaks from the (220) or (200) planes of the γ phase attributed to the main or sub-layers, respectively, can be observed. The peaks from the (311) and (111) planes of the γ phase are also measured. However, these peaks are significantly smaller than those of the (220) and (200), indicating that the rods have a strong crystallographic texture. It is noted that the peak attributed to the (110) plane of the γ' and γ'' phases is not detected in all rods. This result is consistent with electron diffraction analysis using a TEM (Fig. 3) and indicates that the γ ' and γ'' phases are not formed in the all rods.

Fig. 8(b) shows variation in ε_{220} and ε_{200} as a faction of applied true stress (σ_{app}). The deformation behavior of the rods can be divided into three stages according to the deformation state of each layer. In stage I up to $\sigma_{app} \simeq 410$ MPa, ε_{220} and ε_{200} of the main and sub-layers, respectively, increase linearly with increasing σ_{app}. This means that the main and sub-layers undergo elastic deformation in stage I. The difference in values of the slope between ε_{220} and ε_{200} is due to the elastic anisotropy [58]. The diffraction elastic constants (E_{hkl}) for the <110>-oriented main and <100>-oriented sub-layers evaluated by the slopes are 189 GPa and 161 GPa, respectively. On the other hand, in stage II, the slopes of ε_{220} of the main layer start to decrease in all rods when σ_{app} exceeds 410 MPa. In contrast, the slopes of ε_{200} of the sub-layer increase in the stage. In stage III, a further increase in σ_{app}

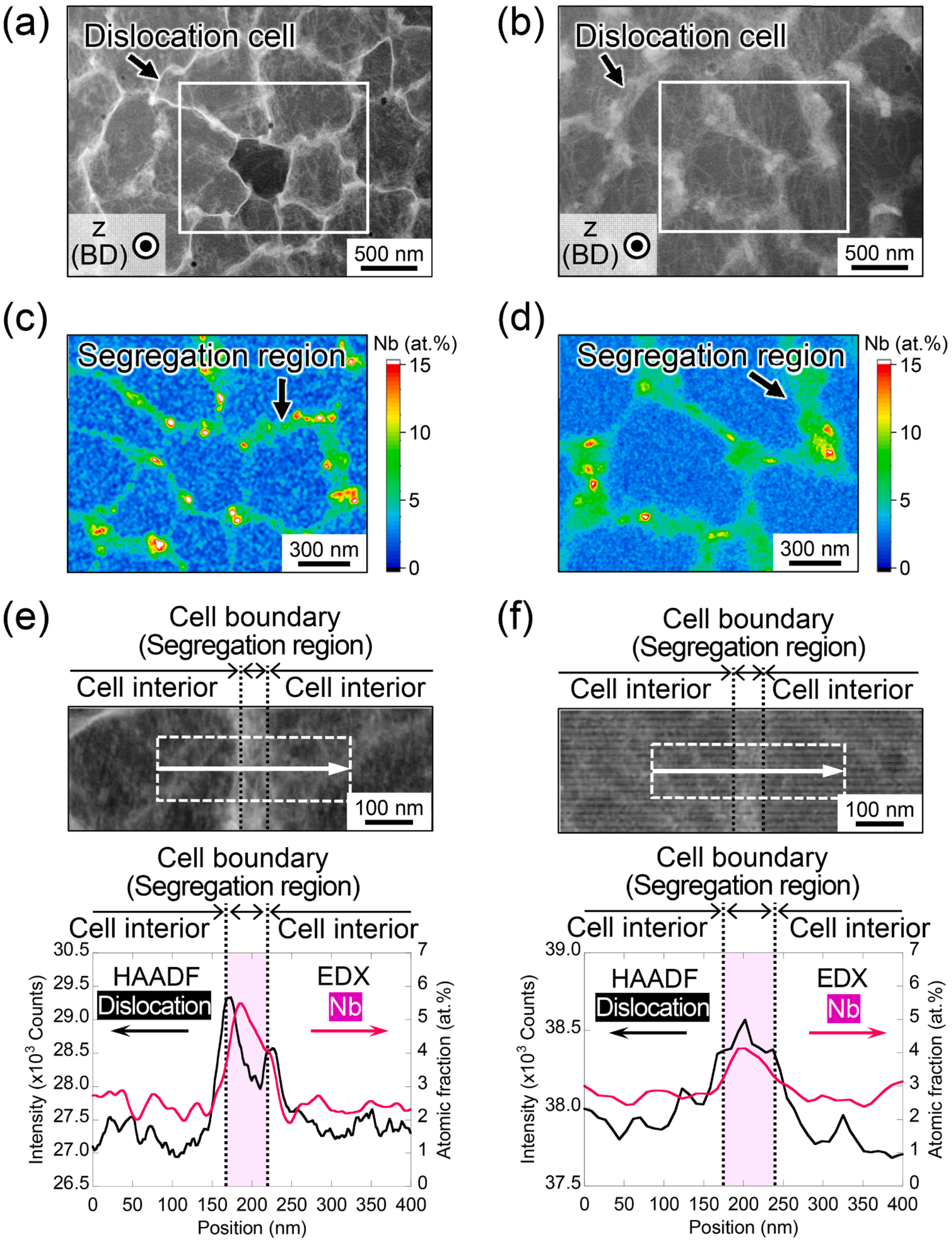

Fig. 6. Typical STEM-HAADF images of the dislocation cell (a), (b) and Nb concentration maps (areas marked by white square in (a), (b)) (c), (d) of the sub-layer in low (a), (c) and high (b), (d) ED rods. (e), (f) Typical STEM-HAADF images, Nb concentration and STEM-HAADF contrast intensity profiles along the white arrow indicated in the images of the type I (e) and II (f) cell boundaries.

causes to the decrease in slopes of ε_{200}. Same behavior was also obtained in a crystal plasticity FEM analysis. Fig. 9(a) shows calculated lattice strain (ε_{Chkl}) of the main (ε_{C220}) and sub-layers (ε_{C200}) as a function of the true stress. It is demonstrated that both ε_{C220} and ε_{C200} of the main and sub-layers increase linearly with increasing the true stress during stage I. However, in stage II (start from black arrow), the slope of ε_{C220} and ε_{C200} becomes smaller and larger, respectively, than those in stage I. Furthermore, as observed in the experimental result, further stress (white arrow) is necessary to reduce the slope of ε_{C200} of the sub-layer (Stage III). Fig. 9(b) displays average slip rate (R_{slip}) indicating the activity of the {111}<110> slip in each layer. In stage I, the main and sub-layers undergo elastic deformation, resulting in their R_{slip} being zero. In stage II, an increase in R_{slip} of the main layer is observed, indicating that only the main layer starts plastic deformation. The high R_{slip} in both layers at stage III implies that both layers deform plastically. These results obtained by the *in-situ* ND and numerical analyses indicate that the main layer undergoes plastic deformation prior to the sub-layer. The micro-yielding phenomenon, in which plastic deformation begins in the main layer before the onset of macroscopic yield, can also be observed from stress partition between the main and sub-layers. The stresses (σ_{hkl}) partitioned in the main (σ_{220})) and sub-layers (σ_{200}) were calculated by Eq. (5).

$$\sigma_{hkl} = E_{hkl}\varepsilon_{hkl} \tag{5}$$

Fig. 8(c) shows σ_{220} and σ_{200} of high ED rod as a function of applied true strain (ε_{app}), along with applied stress-strain (*S-S*) curve of the rod. It should be noted that these curves are corresponding to *S-S* curves of the main and sub-layers. The main layer reaches its yield point (black arrow) before the specimen yields macroscopically (stage II). On the other hand, the sub-layer continues to undergo elastic deformation in stage II and reaches its yield point (white arrow) simultaneously with

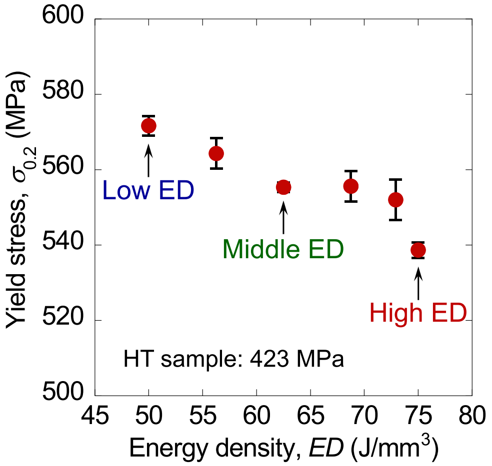

Fig. 7. Macroscopic $\sigma_{0.2}$ of Inconel 718 rods with the hierarchical microstructure fabricated by L-PBF as a function of *ED*.

the macroscopic yield stress of the specimen (stage III). This unique deformation behavior induces a drastic increase in σ_{200} of the sub-layer in stage II due to the elastic interaction between the main and sub-layers.

It is interesting to note that the deformation stress of the sub-layer increases with decreasing *E*, as shown in Fig. 8(d). For example, the sub-layers of high and low ED rods start plastic deformation at σ_{app} of approximately 539 MPa and 575 MPa, respectively. Table 4 presents the deformation stresses of the main and sub-layers and the macroscopic $\sigma_{0.2}$ of each rod. The deformation stress of the sub-layer is in good agreement with $\sigma_{0.2}$ of each rod, whereas that of the main layer is approximately 410 MPa which is much lower than $\sigma_{0.2}$ and is independent of *ED*. This finding implies that not only the wide main layer but also the narrow sub-layer should deform plastically for the macroscopic yielding of the alloys with the CLM. Consequently, the macroscopic $\sigma_{0.2}$ of the alloys is determined by the strength of the sub-layer.

3.2.3. Microscopic strength of the main and sub-layers

To better understand the differences in deformation stress between the main and sub-layers, the strength of each layer was investigated via nanoindentation tests. Fig. 10 shows the average nanoindentation hardness (H_{nano}) of the main and sub-layers in low, middle and high ED rods, measured at the central area of each layer. Although H_{nano} of the main layer tends to increase slightly with decreasing *ED*, there is no statistical difference according to the Tukey's HSD test ($p_T > 0.05$). In contrast, H_{nano} of the sub-layer increases significantly with decreasing *ED* ($p_T < 0.001$). These results correspond reasonably well with the *ED* dependences of the deformation stress of the main and sub-layers, as revealed by the *in-situ* ND analyses (Fig. 8, Table 4). Moreover, it should be noted that H_{nano} of the main and sub-layers of all rods are at least 18 % higher than those of HT sample (approximately 3.5 GPa (for both main and sub-layers)) without the cellular structure. This clearly indicates that the nanoscale cellular structure significantly contributes to the strengthening of each layer.

4. Discussion

The effects of *ED* on the morphology of the unique hierarchical microstructure of Inconel 718 rods fabricated by the L-PBF process were examined. The variations in the morphology of the CLM such as a crystallographic orientation and a width of each layer are nearly independent of *ED* in the range of 50.0–75.0 J/mm^3. However, λ of the nanoscale cellular structure formed in the sub-layer decreases markedly with decreasing *ED*. Further detailed analyses of the cellular structure revealed that the dislocation cell wall is located at both edges of the segregation region (type I cell boundary), except in high ED rod. In contrast, the type II cell boundary consisting of the overlapping dislocation cell and segregation region is formed in high ED rod. Moreover, *in-situ* ND study suggests that the macroscopic tensile strength of the rods is strongly affected by the deformation stress of the sub-layer.

The formation mechanism of the cellular structure is discussed based on detailed observation results of the cell boundary and solidification conditions, together with CtFD simulations. Furthermore, the relationships between the microstructure and strength of the alloys are also discussed particularly focusing on the role of the CLM in the deformation behavior and a new strengthening mechanism caused by the cellular structure.

4.1. Microstructural evolution

4.1.1. Formation mechanism of the cellular structure

As shown in Fig. 2(g) and (h), the columnar cellular structure is formed parallel to the solidification direction of each area. In addition, it was clarified that the cell boundary is a LAGB with a segregation of the specific elements, as shown in Figs. 3(c)–(e) and 4. These findings indicate that the formation of the cellular structure is attributed to dendritic solidification. However, it is difficult to explain formation of the dislocation cell wall, another important feature of the cellular structure, solely in terms of dendritic solidification. It is well known that a large thermal stress (residual stress) is developed in the course of the L-PBF process due to the super-rapid cooling after solidification and exceeds the yield stress of the alloys [59,60]. Therefore, a large number of dislocations are introduced in the rods to decrease the residual stress, which leads to the formation of columnar dislocation cells.

Fig. 11 shows schematic illustrations of the formation mechanism of the cellular structure. The cell formation is divided into two stages: solidification (Fig. 11(a)) and cooling (Fig. 11(b)). During dendritic solidification in the melt pool, the dendrite grains (cells) grow preferentially so that <100> direction is parallel to the heat flow. As in typical dendritic solidification, each dendrite grain has a misorientation of several degrees, thereby resulting in the formation of a LAGB containing geometrically necessary dislocations (GNDs) (Fig. 11(a) I). In general, GNDs are periodically introduced at the LAGBs, depending on the misorientation angle [61]. However, the cell wall with tangled dislocations is not directly formed by the GNDs because the number of GND at the LAGBs is not large enough to form the dislocation cell. Furthermore, Nb, Mo and Ti with equilibrium partition coefficients (k_0) <1 are condensed in the liquid phase at the dendrite tip which is the interface between the liquid and solid phases, while Cr and Fe with k_0 greater than 1 are enriched in the solid phase. Consequently, a segregated region with high amounts of Nb, Mo and Ti is formed at the cell boundary (Fig. 11(a) II). Concentration ratios of the alloying elements between the cell boundary (segregation region) and the cell interior ($k_{B/I}$) evaluated from STEM-EDX analyses are listed in Table 3. These values are in good agreement with k_0 for each element in the γ matrix calculated using Thermo-Calc [62]. The $k_{B/I}$ of Nb has the largest deviation from 1, suggesting that Nb has the highest partitioning tendency. After solidification, super-rapid cooling causes formation of thermal stress, which results in the introduction of numerous dislocations through stress relaxation (Fig. 11(b) I). The large difference in Nb content between the segregation region and cell interior has a pronounced effect on the motion of the dislocations introduced in this stage. The enrichment of Nb of which atomic radius is approximately 18 % larger (146 pm) than that of Ni (124 pm), causes a large lattice strain and increases the shear modulus of the segregation region. Therefore, solid-solution strengthening becomes stronger in the segregation region than that in the cell interior, thereby preventing the penetration of the dislocation into the cell boundary. Moreover, the segregation of Nb decreases a stacking fault energy (SFE) of the cell boundary region [63]. Thus, the stacking fault between the partial dislocations widens when the dislocations penetrate into the segregation region [64]. Rodary et al. performed molecular dynamics calculations and found that the addition of only 3 at

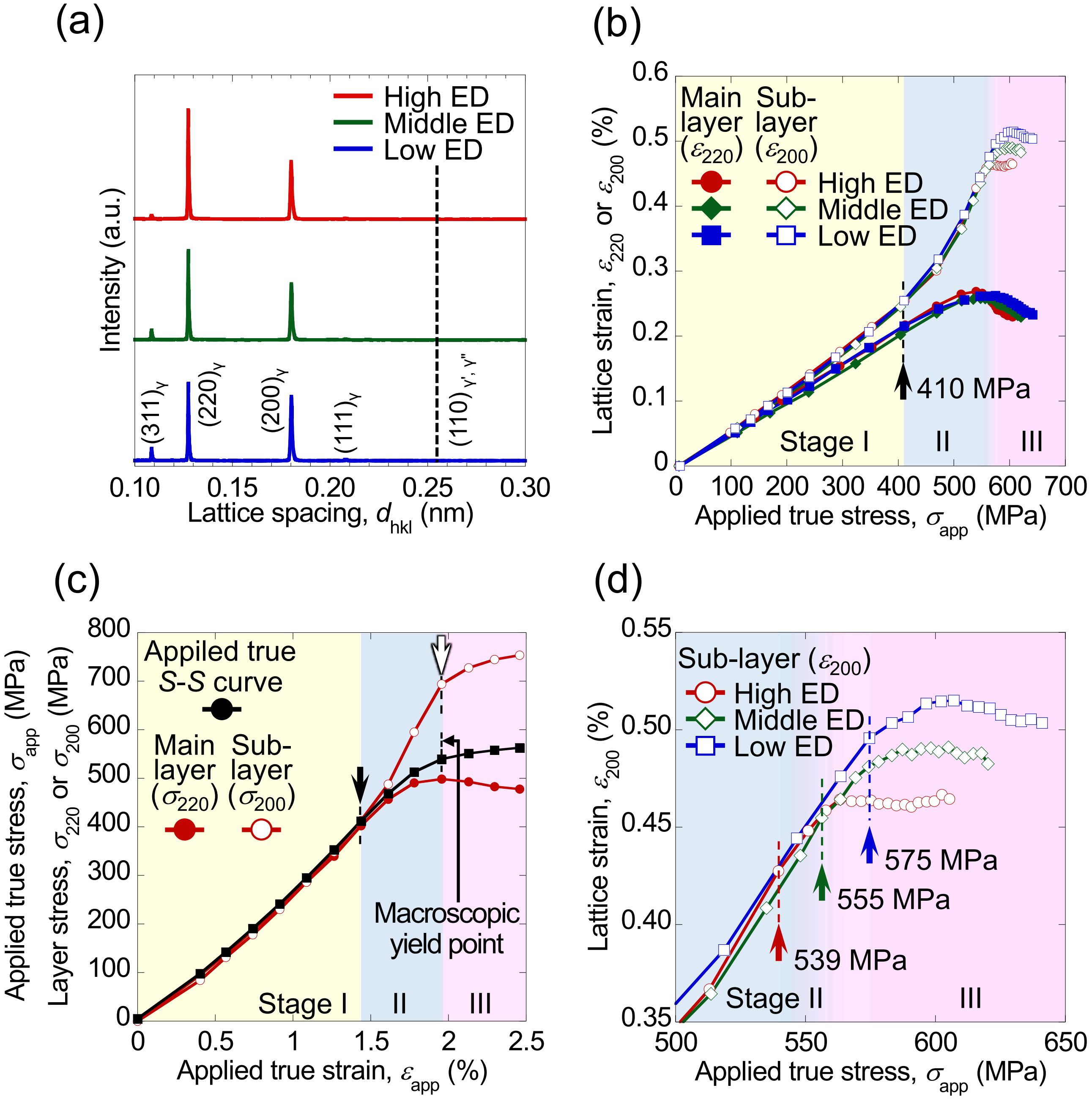

Fig. 8. (a) ND patterns of low, middle and high ED rods taken from BD before tensile deformation. (b)Variations in ε_{220} (main layer) and ε_{200} (sub-layer) of low, middle and high ED rods as a function of σ_{app} measured by the *in-situ* ND analyses. (c) Variations in σ_{app}, σ_{220} (main layer) and σ_{200} (sub-layer) of high ED rod as a function of ε_{app}. (d) Enlarged view of the region in which the sub-layer yielded in (b).

% of Al which lowers SFE of pure Ni reduces the velocity of dislocation glide in Ni alloys by more than one order of magnitude [65]. This study suggests that the glide velocity of the dislocations entering the segregation region decreases rapidly. This may also lead to the accumulation of the dislocations at the edge of the segregation region. In addition, when the dislocation exits the segregation region to the cell interior with a higher SFE, the width of the extended dislocation must be narrower. Therefore, dislocation requires further shear stress to leave the segregation region, depending on the difference in the SFE of each region [66]. In this way, the dislocations introduced to decrease the residual stress are accumulated around the segregation region, resulting in the formation of type I cell boundary at both edges of the segregation region (Fig. 11(b) II). Formation mechanism of type II cell boundary is discussed in 4.1.2.

4.1.2. *Effect of ED on the morphology and characteristics of the cellular structure*

As shown in Fig. 2(i), the morphology of the cellular structure strongly depends on *E*. λ decreases with decreasing *E*, and this tendency is more pronounced in the sub-layer than in the main layer. The formation of the cellular structure begins with rapid dendritic solidification without secondary arms. Therefore, the morphology of the cellular structures is considered to be influenced by solidification conditions such as *G* and *CR*, which are supposed to vary depending on *E*.

The effects of *ED* on *G* and *CR* of the melt pool were numerically analyzed using a CtFD simulation. Fig. 12(a) and (b) show *ED* dependences of *G* and *CR* at the central areas of the main and sub-layers, respectively. Although *G* does not change significantly in both areas, *CR* increases with decreasing *E*. The increase in *CR* can be attributed to

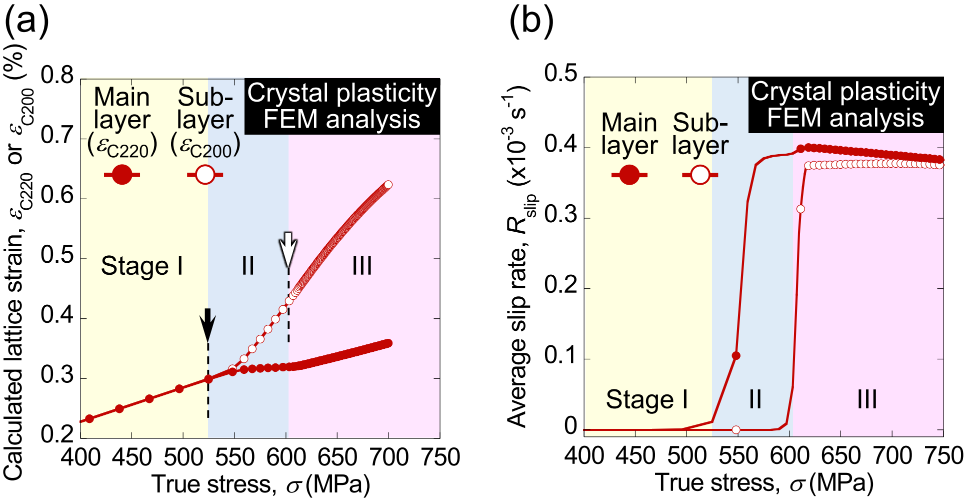

Fig. 9. ε_{C220} (main layer) and ε_{C200} (sub-layer) (a) and R_{slip} (b) around the yield points of the main and sub-layers calculated using the crystal plasticity FEM analysis.

Table 4
Deformation stresses of the main and sub-layers and macroscopic $\sigma_{0.2}$ of low, middle and high ED rods.

	Low ED	Middle ED	High ED
Deformation stress of main layer (MPa)	410	404	412
Deformation stress of sub-layer (MPa)	575	555	539
Macroscopic $\sigma_{0.2}$ (MPa)	572	555	539

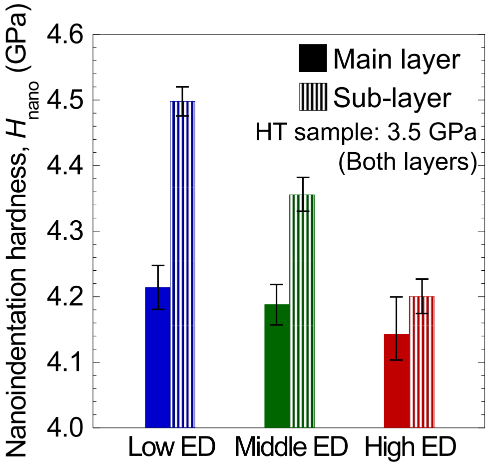

Fig. 10. H_{nano} of the central areas of the main and sub-layers in low, middle and high ED rods.

the decrease in the maximum temperature of the melt pool, caused by the decrease in *E*. It should be noted that the increase in *CR* is particularly taken place in the sub-layer, as shown in Fig. 12(b). This phenomenon is thought to be related to the *ED* dependence of the melt pool shape. The depth of the melt pool depends on *ED* more significantly than the width (Fig. S3). The rapid shallowing of the melt pool at low *ED* leads to the fast *CR* in the sub-layer [67].

The Lipton-Glicksman-Kurz (LGK) model shows the relationship between primary dendrite arm spacing (λ_{PDAS}) and solidification conditions [68]. This model is expressed as

$$\lambda_{PDAS} = \left(-\frac{72\pi^2 \Gamma_{SL} D_L \Delta T_0}{k_0} \right)^{1/4} G^{-1/2} R^{-1/4} \tag{6}$$

where Γ_{SL}, D_L, ΔT_0 and R represent the Gibbs–Thomson coefficient, diffusion coefficient in the liquid phase, degree of supercooling at the dendrite tip and solidification rate, respectively. It is clear from Eq. (6) that λ_{PDAS} corresponding to cell spacing increases linearly with increasing $G^{-1/2}R^{-1/4}$ defined as the LGK parameter. Fig. 12(c) shows the variations in the LGK parameters with *ED* at the central areas of the main and sub-layers. Note that the values of *R* are calculated by dividing *CR* by *G*. The LGK parameters decrease approximately 10 % and 18 % in main and sub-layers, respectively, with decreasing *ED* from 75 J/mm^2 to 50 J/mm^3. The more marked decrease in the LGK parameter in the sub-layer is due to the strong *ED* dependence of *CR*. As summarized in Fig. 12 (d), the average λ measured via microstructure observation (Fig. 2(i)) and the LGK parameters at central area of each layer have a linear relationship regardless of *ED* and whether it is the main or sub-layer. This result indicates that the *ED* dependence of λ is caused by variations in the solidification conditions.

Another effect of increased *ED* on the morphology of the cellular structure is the formation of the type II cell boundary in high ED rod. In type II boundary, wide dislocation cell overlaps with the segregation region with relatively low Nb concentration (Fig. 6(f)). Dendritic solidification and subsequent stress relaxation during cooling are insufficient to explain the formation of the type II cell boundary. As reported in the numerical simulation studies on thermal history during the process, a heat affected zone with a range of several tens to hundreds of micrometers is formed in the vicinity of the melt pool [69]. This temperature distribution in the zone shifts to higher temperatures and the zone extends over a wider area with increasing *E*. Therefore, in the case of high *ED* conditions, Nb enriched in the segregation region is diffused by the thermal effect from the melt pool during adjacent and/or upper layer beam scanning. This thermal effect also activates the motion of the dislocation in the dislocation cells. When Nb concentration in the segregation region decreases below a certain value, the dislocations at the type I boundary can penetrate into the region, thereby resulting in the formation of the type II cell boundary.

4.2. Effect of the hierarchical microstructure on tensile strength

4.2.1. Deformation behavior of Inconel 718 rods with CLM

The deformation behavior of metallic materials depends strongly on their crystallographic orientations. In particular, the anisotropy of plastic deformation follows the Schmid law. As shown in Fig. 2(a)–(c), the three rods with different *ED* values have CLM, and the crystallographic orientations of the main and sub-layers with respect to the load axis are ⟨110⟩ and ⟨100⟩ orientations, respectively. The maximum Schmid factors for {111}<110> slip which is the primary slip system of the fcc structure at ⟨110⟩ and ⟨100⟩ orientations are the same at 0.408.

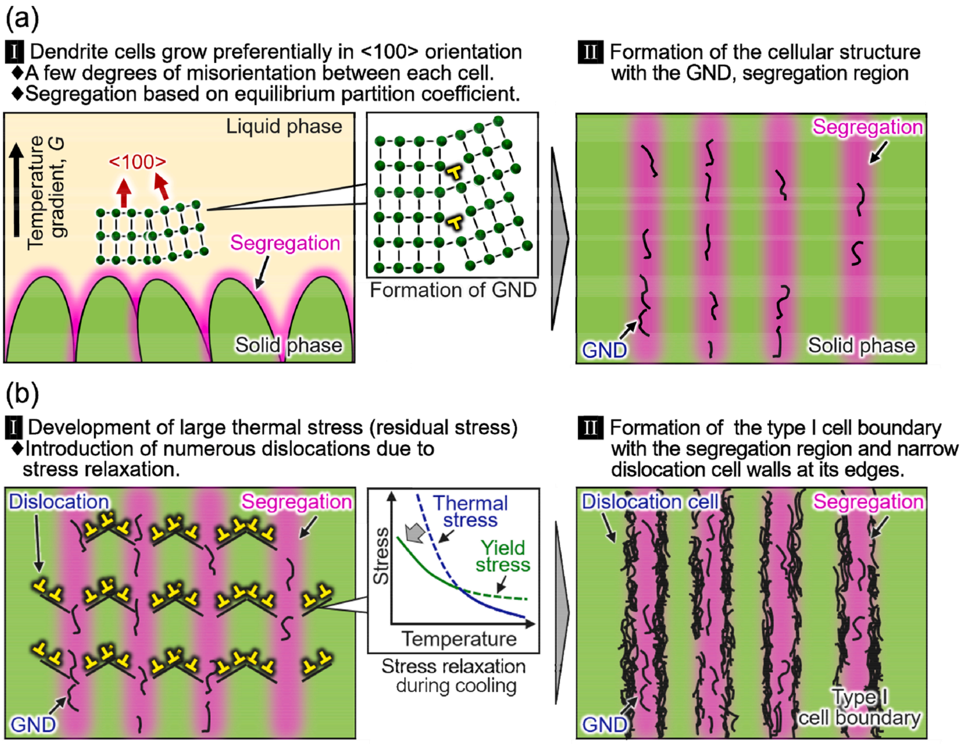

Fig. 11. Schematic illustrations showing formation mechanism of the cellular structure during solidification (a) and cooling (b).

Therefore, according to the Schmid law, if the critical resolved shear stresses (CRSSs) of $\{111\}<110>$ slip in the main and sub-layers are also the same, both the layers should start to deform plastically under the same applied stress. Since H_{nano} of the main and sub-layers of high ED rod are comparable, the strength and CRSS of each layer are also expected to be similar (Fig. 10). However, the *in-situ* ND experiments reveal that the main layer exhibits micro-yielding prior to the sub-layer in high ED rod (Fig. 8). The elastic anisotropy may contribute to the preferential deformation of the main layer. As described above, the diffraction elastic constants of the $<110>$-oriented main layer (189 GPa) is higher than that of $<100>$-oriented sub-layers (161 GPa). If a load is applied parallel to BD, the local strains in the main and sub-layers along the loading direction should be the same. Thus, the stress partitioned in the main layer with high Young's modulus is greater than that in the sub-layer according to Hooke's law. Therefore, the main layer starts plastic deformation earlier than the sub-layer. In CLM alloys, both the main and sub-layers must be plastically deformed in order to reach macroscopic yielding (Table 4). Thus, the delay in the plastic deformation of the sub-layer leads to macroscopic strengthening at an early stage of deformation and increases macroscopic $\sigma_{0.2}$.

This strengthening due to the CLM is more pronounced for low and middle ED rods. As indicated in Fig. 10, H_{nano} of the main layer is insensitive to *ED*, while that of the sub-layer increases significantly with decreasing *ED*. Consequently, the strength and CRSS of the sub-layer are higher than those of the main layer in low and middle ED rods. Therefore, the plastic deformation of the sub-layers in these rods is further delayed compared with that in high ED rod, resulting in a significant increase in the macroscopic strength of the alloys (Fig. 8). This means that the strength of the CLM alloys can be improved by further increase in the strength of the sub-layer.

4.2.2. Influence of the cellular structure on the strength

As described in Fig. 10, the main and sub-layers are strengthened by the cellular structure. Therefore, let us discuss the relationship between morphology of the cellular structure and the macroscopic strength of rods, focusing on the spacing of the cellular structure. The relationship between average H_{nano} and $\lambda^{-1/2}$ of the main and sub-layers for low ED, middle and high ED rods are shown in Fig. 13(a). Except for high ED rod, H_{nano} value exhibits a good linear relationship with $\lambda^{-1/2}$ for both layers, indicating that the Hall-Petch relation holds between H_{nano} and λ. Fig. 13(b) shows the Hall–Petch plots of macroscopic $\sigma_{0.2}$ and $\lambda^{-1/2}$ of the sub-layer for all tensile tested rods. The macroscopic strength of the alloys which excludes the high ED rod increases with decreasing λ of the sub-layer, clearly satisfying the Hall–Petch relationship as follows,

$$\sigma_{0.2} = \sigma_0 + k\lambda^{-1/2} \tag{7}$$

where σ_0 and k represent the yield stress of the rods without the cellular structure and the Hall–Petch coefficient, respectively. This result suggests that the cellular structure can cause refinement strengthening through the accumulation of mobile dislocations at cell boundary, similar to the high-angle grain boundary (HAGB). Here, it should be noted that the type II cell boundary is observed only in high ED rods, while the cell boundary in middle and low ED rods is type I (Fig. 6). This means that the Hall-Petch relation shown in Fig. 13 corresponds to the type I boundary. Furthermore, it should also be noted that the k value in Fig. 13(b) is 77 MPa•μm$^{1/2}$, which is comparable to or higher than that reported for polycrystalline pure Ni (68 MPa•μm$^{1/2}$) [70]. The cellular structure with the type I cell boundary has a high strengthening ability, though that is a kind of LAGB. These results indicate that the formation of the type I cell boundary in the sub-layer results in significant strengthening of the as built rod. Moreover, the intercept of the Hall–Petch line, which corresponds to σ_0 in Eq. (7), is 463 MPa, which is approximately 10 % higher than $\sigma_{0.2}$ of HT sample (423 MPa). This is because not only the cellular structure but also the dislocations in the cell interior were relaxed from approximately 3.0×10^{14} m^{-2} (as built low ED rod) to 6.5×10^{12} m^{-2} in HT sample (Fig. S2). This suggests that the dislocation in the cell interior also contributes to the strengthening of the rods.

As mentioned above, the Hall-Petch relation shown in Fig. 13 corresponds to the type I cell boundary. On the other hand, high ED rod contains the type II boundary. It is interesting to note that H_{nano} and $\sigma_{0.2}$

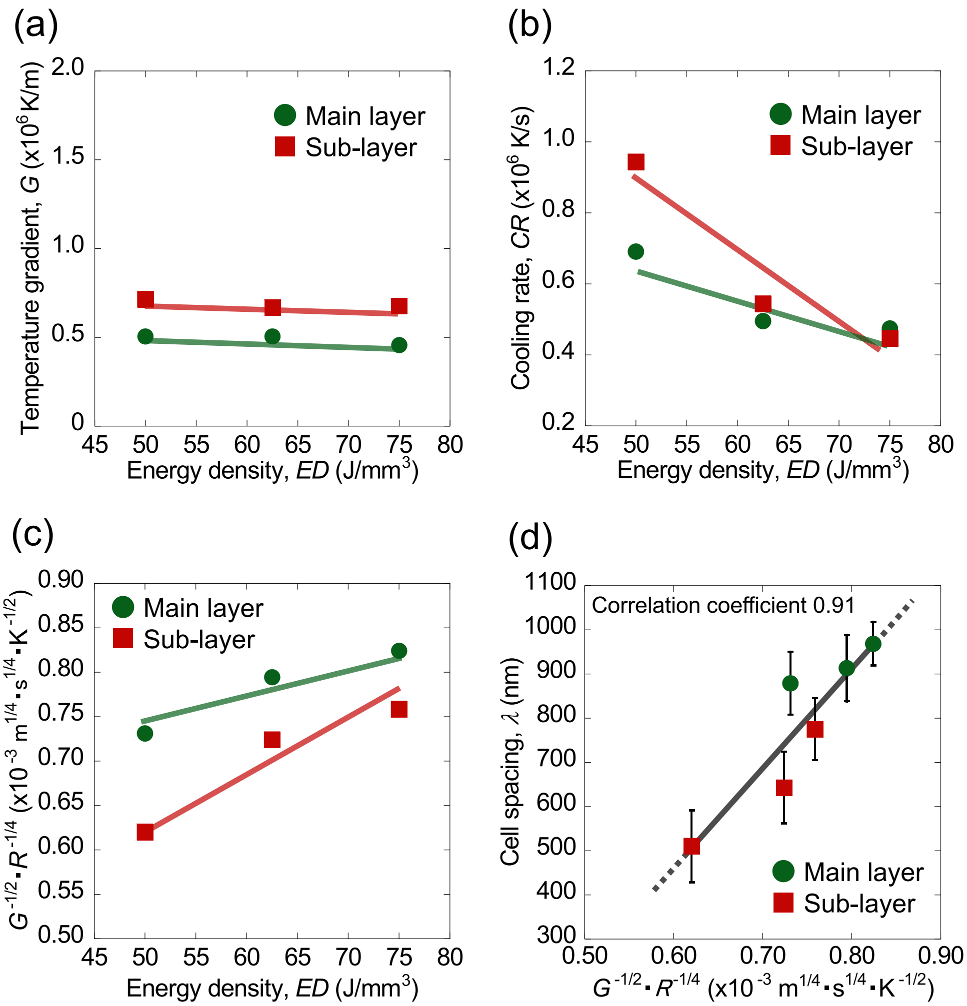

Fig. 12. Variations in G (a) and CR (b) at the central areas of the main and sub-layers calculated by the CtFD simulations as a function of ED. (c) LGK parameters of the main and sub-layers as a function of ED. (d) Relationship between the average λ and LGK parameters.

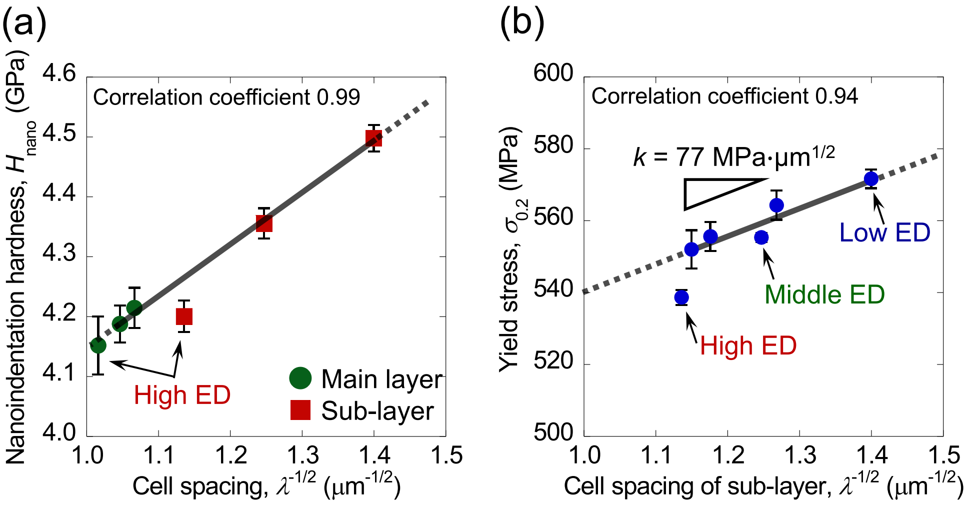

Fig. 13. Relationships between average H_{nano} and $\lambda^{-1/2}$ of the main and sub-layers for low, middle and high ED rods (a) and $\sigma_{0.2}$ and $\lambda^{-1/2}$ of the sub-layer for tensile tested rods.

of high ED rods with the type II cell boundary are lower than those expected from the Hall–Petch plots for the type I cell boundary in low and middle ED rods (Fig. 13). These results indicate that the strengthening ability of the cellular structure depends on not only λ but also the type of cell boundary. Therefore, the strengthening mechanism by the cellular structure is discussed in the next section, focusing on the type of cell boundary.

4.2.3. *Strengthening mechanism afforded by the cellular structure*

As shown in Fig. 13(b), $\sigma_{0.2}$ of low and middle ED rods can be expressed by the Hall–Petch relationship focusing on λ of the sub-layer. This result indicates that the cell boundary acts as a strong obstacle to the motion of mobile dislocations. In the case of the type I cell boundary wherein the dislocation cell wall is formed at the edges of the segregation region, the mobile dislocations introduced by the deformation cannot pass through the dislocation cell wall and the segregation region. As a result, the mobile dislocations accumulate outside of them (Fig. 14(a)). This is the same phenomenon as the dislocation pile-up at HAGB. For the shear deformation to be transmitted to adjacent cell, a new dislocation source must be activated at the position r_{typeI} away from the tip of piled up dislocations, where is the opposite side across the cell boundary region (Fig. 14(a)). When considered in the same way as the Hall–Petch strengthening, the shear stress (τ_{B}) on the slip plane caused by the dislocation piled-up at the dislocation cell wall is given by [71],

$$\tau_{\mathrm{B}} = \left(\frac{\lambda}{4r}\right)^{1/2}(\tau - \tau_0) \tag{8}$$

where r is a distance from the leading dislocation, τ and τ_0 represent the applied shear stress and shear stress hindering the motion of dislocation, respectively. Note that τ_0 is the stress similar to the lattice resistance of the Peierls potential. When τ_{B} at r_{tyepI} exceeds the critical stress (τ_{C}) for the formation of the new dislocation source, the shear deformation propagates across the cell boundary, resulting in yielding (Fig. 14(a)). $\sigma_{0.2}$ and k that represents the strengthening ability of the cell boundary can be expressed in Eqs. (9) and (10), respectively, using the Taylor factor (M_{T}) and Eq. (7) [72].

$$\sigma_{0.2} = M_{\mathrm{T}}\tau_0 + 2M_{\mathrm{T}}\tau_{\mathrm{C}}\sqrt{r}\lambda^{-1/2} = \sigma_0 + k\lambda^{-1/2} \tag{9}$$

$$k = 2M_{\mathrm{T}}\tau_{\mathrm{C}}\sqrt{r} \tag{10}$$

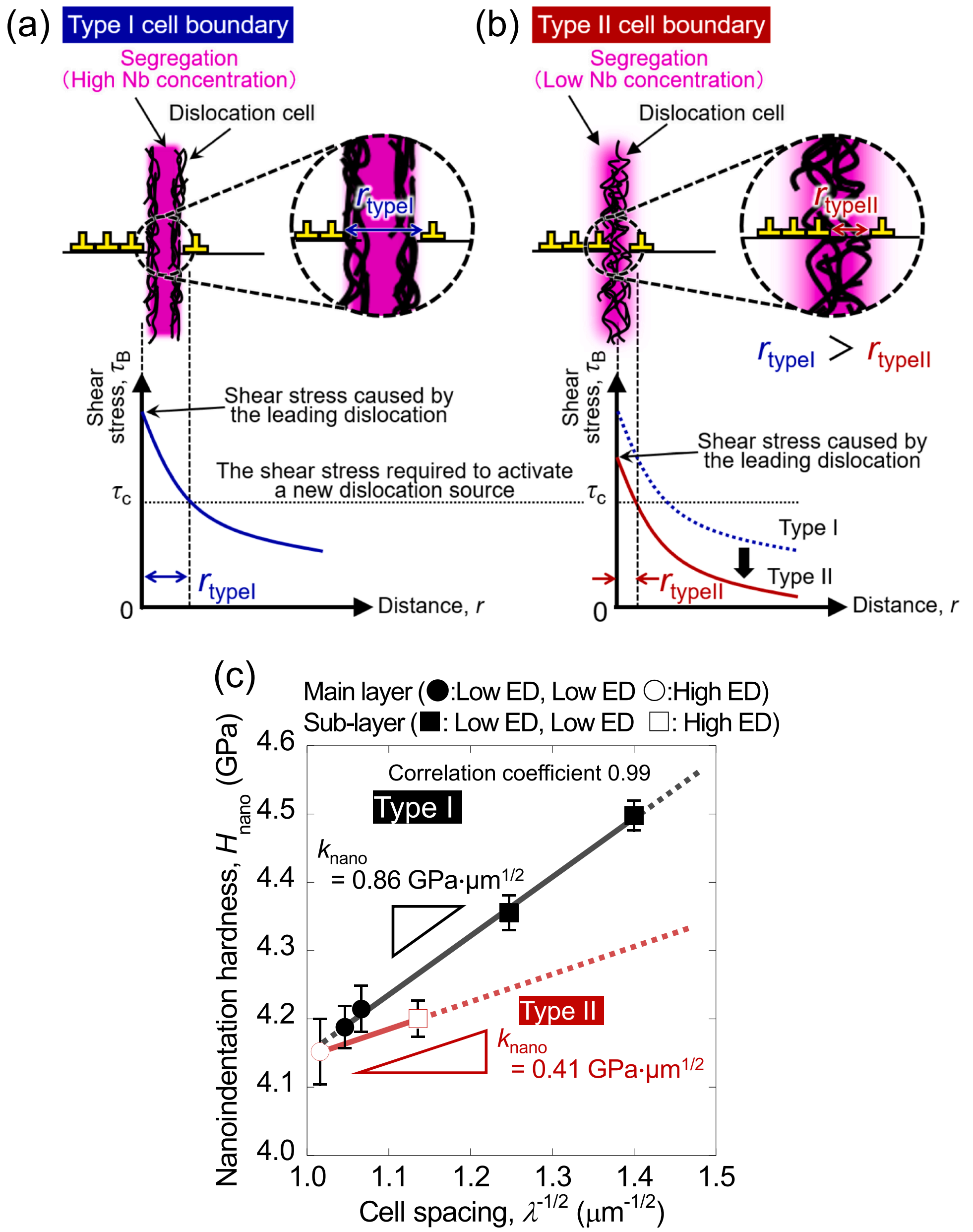

Fig. 14. Schematic illustrations of the strengthening mechanisms caused by the type I (a) and II (b) cell boundaries. (c) Relationship between H_{nano} and $\lambda^{-1/2}$ for low, middle and high ED rods containing the type I and II cell boundaries.

Eq. (10) indicates that the strengthening ability of the cell boundary depends on r. This can account for the difference in strengthening ability between the type I and II cell boundaries. At the type II cell boundary observed in high ED rod, the mobile dislocations can enter the segregation region because the Nb concentration is decreased by approximately 1.5 at % due to the thermal effect from the melt pool of the adjacent and/or upper layer beam scanning (Fig. 6(e), (f)). In this case, the mobile dislocations accumulate at the dislocation cell wall formed within the segregation region (Fig. 14(b)). As a result, the distance r_{typeII} from the leading dislocation to the new dislocation source in the adjacent cell is shorter than r_{typeI}. On the other hand, τ_C is constant regardless of the type of cell boundary. Therefore, at the type II cell boundary, τ_B at r_{typeII} exceeds τ_C at lower τ, compared with type I, resulting in low strength of high ED rod (Fig. 13). Moreover, according to Eq. (10), k for the type II cell boundary should be lower than that of the type I cell boundary. Thus, the Hall–Petch relationships of the type I (low and middle ED rods) and II (high ED rod) cell boundaries between the H_{nano} and $\lambda^{-1/2}$ of the main and sub-layers of each rod are shown in Fig. 14(c). The intercepts of the Hall-Petch lines for the type I and II cell boundaries are comparable to each other (type I: 3.3 GPa, type II: 3.7 GPa). In contrast, as expected from Eq. (10), the slope (k_{nano}) for the type II (0.41 GPa•μm$^{1/2}$) cell boundary in high ED rod is significantly lower than that of type I (0.86 GPa•μm$^{1/2}$) in low and middle ED rods. This result indicates that the type I cell boundary induces more effective refinement strengthening, compared with the type II cell boundary. Thus, the cell boundary type as well as the cell spacing plays an important role in strengthening by the nanoscale cellular structure formed by the L-PBF process.

5. Conclusions

The effects of *ED* on the morphology of the CLM and nanoscale cellular structure in Inconel 718 alloys fabricated by the L-PBF process were investigated. The deformation behavior and strengthening mechanism of the alloys were also examined, focusing on the morphology of the cellular structure. The following conclusions were drawn from the present study:

1. The CLM consisting of the main layer with <110>//BD orientation and the sub-layer with <100>//BD orientation can be obtained by L-PBF with appropriate *ED* values in the range of 50.0 J/mm^3 to 75.0 J/mm^3. In this *ED* range, the width of each layer is constant regardless of *ED*.
2. The boundary of the cellular structure is a LAGB accompanied with numerous dislocations and segregation of Nb, Mo and Ti. The dendritic solidification contributes to the formation of the segregation region and subsequent stress relaxation during cooling of the columnar solidified area leads to the development of the dislocation cell wall. The dislocations are basically located at both edges of the segregation region (type I cell boundary).
3. *CR* of the melt pool increases with decreasing *ED*, resulting in a decrease in λ, which is more pronounced in the sub-layer. On the other hand, high *ED* condition leads to the formation of the cellular structure with dislocations penetrating into the segregation region (type II cell boundary) in addition to an increase in λ.
4. *In-situ* ND study proves that the main layer in the CLM undergoes plastic deformation prior to the sub-layer. A stress partitioning between the main and sub-layers occurs at an early stage of deformation, and consequently the elastic deformation of the sub-layer contributes to the macroscopic strengthening.
5. Although the cell boundary is a LAGB, significant Hall–Petch strengthening can be obtained. This is because the dislocation cell walls formed in the vicinity of the segregation region act as a pile-up site for the mobile dislocations introduced by the deformation. The strengthening ability of the cellular structure depends on the type of cell boundary.
6. The type I cell boundary provides significant strengthening comparable to or greater than that caused by large-angle grain boundaries, thereby increasing the macroscopic strength of the rods through hardening of the sub-layer.

CRediT authorship contribution statement

Ken Cho: Writing – review & editing, Writing – original draft, Visualization, Validation, Methodology, Investigation, Formal analysis, Data curation, Conceptualization. **Kippei Yamashita:** Validation, Investigation, Formal analysis. **Shinnosuke Kakutani:** Validation, Investigation, Formal analysis. **Takuma Saito:** Investigation, Formal analysis. **Taisuke Sasaki:** Writing – review & editing, Validation, Formal analysis. **Katsuhiko Sawaizumi:** Software. **Masayuki Okugawa:** Writing – review & editing, Validation, Software. **Yuichiro Koizumi:** Writing – review & editing, Software. **Tsuyoshi Mayama:** Writing – review & editing, Validation, Software. **Taichi Kikukawa:** Investigation, Formal analysis. **Ozkan Gokcekaya:** Writing – review & editing, Validation. **Takuya Ishimoto:** Writing – review & editing, Validation. **Hajime Kimizuka:** Writing – review & editing, Validation. **Wu Gong:** Writing – review & editing, Visualization, Formal analysis. **Takuro Kawasaki:** Writing – review & editing, Visualization. **Stefanus Harjo:** Writing – review & editing, Visualization, Formal analysis. **Takayoshi Nakano:** Writing – review & editing, Supervision, Project administration, Methodology, Conceptualization. **Hiroyuki Y. Yasuda:** Writing – review & editing, Supervision, Project administration, Methodology, Conceptualization.

Declaration of competing interest

The authors declare that they have no known competing financial interests or personal relationships that could have appeared to influence the work reported in this paper.

Acknowledgements

This work was supported by CREST-Nanomechanics: Elucidation of macroscale mechanical properties based on understanding nanoscale dynamics of innovative mechanical materials (Grant Number: JPMJCR2194) from the Japan Science and Technology Agency (JST) and Grant-in-Aid for Transformative Research Area (A) (Grant Number: 21H05196) from the Japan Society for the Promotion of Science (JSPS). The neutron diffraction experiments were conducted at the Materials and Life Science Experimental Facility of the J-PARC under a user program (Proposal Number: 2022B0149).

Supplementary materials

Supplementary material associated with this article can be found, in the online version, at doi:10.1016/j.actamat.2025.121696.

Data availability

Data will be made available on request.

References

[1] H. Long, S. Mao, Y. Liu, Z. Zhang, X. Han, Microstructural and compositional design of Ni-based single crystalline superalloys – A review, J. Alloy. Compd. 743 (2018) 203–220, https://doi.org/10.1016/j.jallcom.2018.01.224.

[2] H. Mughrabi, U. Tetzlaff, Microstructure and high-temperature strength of monocrystalline nickel-base superalloys, Adv. Eng. Mater. 2 (2002) 319–326, https://doi.org/10.1002/1527-2648(200006)2:6<319::AID-ADEM319>3.0.CO;2-S.

[3] R. Viswanathan, K. Coleman, U. Rao, Materials for ultra-supercritical coal-fired power plant boilers, Int. J. Press. Vessel. Pip. 83 (2006) 778–783, https://doi.org/10.1016/j.ijpvp.2006.08.006.

[4] R.J. Smith, G.J. Lewi, D.H. Yates, Development and application of nickel alloys in aerospace engineering, Aircr. Eng. Aerosp. Tech. 73 (2001) 138–147, https://doi.org/10.1108/00022660110694995.

[5] A.F. Giamei, D.L. Anton, Rhenium additions to a Ni-base superalloy: effects on microstructure, Metall. Trans. A 16 (1985) 1997–2005, https://doi.org/10.1007/BF02662400.

[6] A. Royer, P. Bastie, M. Veron, In situ determination of γ' phase volume fraction and of relations between lattice parameters and precipitate morphology in Ni-based single crystal superalloy, Acta Mater. 46 (1998) 5357–5368, https://doi.org/10.1016/S1359-6454(98)00206-7.

[7] S. Zhao, X. Xie, G.D. Smith, S.J. Patel, Microstructural stability and mechanical properties of a new nickel-based superalloy, Mater. Sci. Eng. A 355 (2003) 96–105, https://doi.org/10.1016/S0921-5093(03)00051-0.

[8] V.I. Razumovskiy, A.Y. Lozovoi, I.M. Razumovskii, First-principles-aided design of a new Ni-base superalloy: influence of transition metal alloying elements on grain boundary and bulk cohesion, Acta Mater. 82 (2015) 369–377, https://doi.org/10.1016/j.actamat.2014.08.047.

[9] M.M. Attallah, R. Jennings, X. Wang, L.N. Carter, Additive manufacturing of Ni-based superalloys: the outstanding issues, MRS Bull. 41 (2016) 758–764, https://doi.org/10.1557/mrs.2016.211.

[10] Y.L. Kuo, S. Horikawa, K. Kakehi, Effects of build direction and heat treatment on creep properties of Ni-base superalloy built up by additive manufacturing, Scr. Mater. 129 (2017) 74–78, https://doi.org/10.1016/j.scriptamat.2016.10.035.

[11] T. Nakano, Selective laser melting, in: S. Kirihara, K. Nakata (Eds.), Multi-dimensional Additive Manufacturing, Springer, Singapore, 2020, pp. 3–26, https://doi.org/10.1007/978-981-15-7910-3_1.

[12] B. Blakey-Milner, P. Gradl, G. Snedden, M. Brooks, J. Pitot, E. Lopez, M. Leary, F. Berto, A. du Plessis, Metal additive manufacturing in aerospace: a review, Mater. Des. 209 (2021) 110008, https://doi.org/10.1016/j.matdes.2021.110008.

[13] T. Peng, K. Kellens, R. Tang, C. Chen, G. Chen, Sustainability of additive manufacturing: an overview on its energy demand and environmental impact, Addit. Manuf. 21 (2018) 694–704, https://doi.org/10.1016/j.addma.2018.04.022.

[14] T. Nakano, K. Hagihara, Additive manufacturing of medical devices, ASM Handbook 23A (2022) 416–433, https://doi.org/10.31399/asm.hb.v23A.a0006905.

[15] N. Hrabe, T. Quinn, Effects of processing on microstructure and mechanical properties of a titanium alloy (Ti-6Al-4V) fabricated using electron beam melting (EBM), part 2: energy input, orientation, and location, Mater. Sci. Eng. A 573 (2013) 271–277, https://doi.org/10.1016/j.msea.2013.02.065.

[16] H. Amano, T. Ishimoto, R. Suganuma, K. Aiba, S.-H. Sun, R. Ozasa, T. Nakano, Effect of a Helium gas atmosphere on the mechanical properties of Ti-6Al-4V alloy built with laser powder bed fusion: a comparative study with argon gas, Addit. Manuf. 48 (2021) 102444, https://doi.org/10.1016/j.addma.2021.102444Y.

[17] L.E.Rännar Zhong, L. Liu, A. Koptyug, S. Wikman, J. Olsen, D. Cui, Z. Shen, Additive manufacturing of 316L stainless steel by electron beam melting for nuclear fusion applications, J. Nucl. Mater. 486 (2017) 234–245, https://doi.org/10.1016/j.jnucmat.2016.12.042.

[18] R. Shrestha, J. Simsiriwong, N. Shamsaei, Fatigue behavior of additive manufactured 316L stainless steel parts: effects of layer orientation and surface roughness, Addit. Manuf. 28 (2019) 23–38, https://doi.org/10.1016/j.addma.2019.04.011.

[19] M. Okugawa, Y. Ohigashi, Y. Furushiro, Y. Koizumi, T. Nakano, quiaxed grain formation by intrinsic heterogeneous nucleation via rapid heating and cooling in additive manufacturing of aluminum-silicon hypoeutectic alloy, J. Alloy. Compd. 919 (2022) 165812, https://doi.org/10.1016/j.jallcom.2022.165812.

[20] M. Liu, N. Takata, A. Suzuki, M. Kobashi, M. Kato, Enhancement in strength and ductility of laser powder bed fused Al-12Si alloy by introducing nanoscale precipitates, Addit. Manuf. Lett. 1 (2021) 100008, https://doi.org/10.1016/j.addlet.2021.100008.

[21] J. Schwerdtfeger, C. Körner, Selective electron beam melting of Ti-48Al-2Nb-2Cr: microstructure and aluminium loss, Intermetallics 49 (2014) 29–35, https://doi.org/10.1016/j.intermet.2014.01.004.

[22] K. Cho, R. Kobayashi, J.Y. Oh, H.Y. Yasuda, M. Todai, T. Nakano, A. Ikeda, M. Ueda, M. Takeyama, Influence of unique layered microstructure on fatigue properties of Ti-48Al-2Cr-2Nb alloys fabricated by electron beam melting, Intermetallics 95 (2018) 1–10, https://doi.org/10.1016/j.intermet.2018.01.009.

[23] R. Wartbichler, H. Clemens, S. Mayer, Electron beam melting of a β-solidifying intermetallic titanium aluminide alloy, Adv. Eng. Mater. 21 (2019) 1900800, https://doi.org/10.1002/adem.201900800.

[24] W. Zhou, X. Sun, K. Tsunoda, K. Kikuchi, N. Nomura, K. Yoshimi, A. Kawasaki, Powder fabrication and laser additive manufacturing of MoSiBTiC alloy, Intermetallics 104 (2019) 33–42, https://doi.org/10.1016/j.intermet.2018.10.012.

[25] K. Hagihara, T. Nakano, Control of anisotropic crystallographic texture in powder bed fusion additive manufacturing of metals and ceramics—A review, JOM 74 (2022) 1760–1773, https://doi.org/10.1007/s11837-021-04966-7.

[26] V. Yakubov, J.J. Kruzic, X. Li, Heat-resistant intermetallic compounds and ceramic dispersion alloys for additive manufacturing: a review, Adv. Eng. Mater. 24 (2022) 2200159, https://doi.org/10.1002/adem.202200159.

[27] P. Wang, P. Huang, F.L. Ng, W.J. Sin, S. Lu, M.L.S. Nai, Z.L. Dong, J. Wei, Additively manufactured CoCrFeNiMn high-entropy alloy viapre-alloyed powder, Mater. Des. 168 (2019) 107576, https://doi.org/10.1016/j.matdes.2018.107576.

[28] H. Chen, D. Egusa, Z. Li, T. Sasaki, R. Ozasa, T. Ishimoto, M. Okugawa, Y. Koizumi, T. Nakano, E. Abe, Phase-separation induced dislocation-network cellular structures in Ti-Zr-Nb-Mo-Ta high-entropy alloy processed by laser powder bed fusion, Addit. Manuf. 102 (2025) 104737, https://doi.org/10.1016/j.addma.2025.104737.

[29] O. Gokcekaya, T. Ishimoto, Y. Nishikawa, Y.S. Kim, A. Matsugaki, R. Ozasa, M. Weinmann, C. Schnitter, M. Stenzel, H.S. Kim, Y. Miyabayashi, T. Nakano, Novel single crystalline-like non-equiatomic TiZrHfNbTaMo bio-high entropy alloy (BioHEA) developed by laser powder bed fusion, Mater. Res. Lett. 11 (2023) 274–280, https://doi.org/10.1080/21663831.2022.2147406.

[30] Y.S. Lee, M.M. Kirka, J. Ferguson, V.C. Paquit, Correlations of cracking with scan strategy and build geometry in electron beam powder bed additive manufacturing, Addit. Manuf. 32 (2020) 101031, https://doi.org/10.1016/j.addma.2019.101031.

[31] C.A. Biffi, J. Fiocchi1, E. Ferrario, A. Fornaci, M. Riccio, M. Romeo, A. Tuissi, Effects of the scanning strategy on the microstructure and mechanical properties of a TiAl6V4 alloy produced by electron beam additive manufacturing, J. Adv. Manuf. Technol. 107 (2020) 4913–4924, https://doi.org/10.1007/s00170-020-05358-y.

[32] K. Cho, H. Kawabata, T. Hayashi, H.Y. Yasuda, H. Nakashima, M. Takeyama, T. Nakano, Peculiar microstructural evolution and tensile properties of β-containing γ-TiAl alloys fabricated by electron beam melting, Addit. Manuf. 46 (2021) 102091, https://doi.org/10.1016/j.addma.2021.102091.

[33] K. Cho, H. Odo, K. Okamoto, H.Y. Yasuda, H. Nakashima, M. Takeyama, T. Nakano, Improving the tensile properties of additively manufactured β-containing TiAl alloys via microstructure control focusing on cellular precipitation reaction, Crystals 11 (2021) 809, https://doi.org/10.3390/cryst11070809.

[34] T. Kurzynowski, K. Gruber, W. Stopyra, B. Kuźnicka, E. Chlebus, Correlation between process parameters, microstructure and properties of 316 L stainless steel processed by selective laser melting, Mater. Sci. Eng. A 718 (2018) 64–73, https://doi.org/10.1016/j.msea.2018.01.103.

[35] T. Ishimoto, K. Hagihara, K. Hisamoto, S.-H. Sun, T. Nakano, Crystallographic texture control of beta-type Ti-15Mo-5Zr-3Al alloy by selective laser melting for the development of novel implants with a biocompatible low Young's modulus, Scr. Mater. 132 (2017) 34–38, https://doi.org/10.1016/j.scriptamat.2016.12.038.

[36] M. Todai, T. Nakano, T. Liu, H.Y. Yasuda, K. Hagihara, K. Cho, M. Ueda, M. Takeyama, Effect of building direction on the microstructure and tensile properties of Ti-48Al-2Cr-2Nb alloy additively manufactured by electron beam melting, Addit. Manuf. 13 (2017) 61–70, https://doi.org/10.1016/j.addma.2016.11.001.

[37] M. Okugawa, K. Saito, H. Yoshima, K. Sawaizumi, S. Nomoto, M. Watanabe, T. Nakano, Y. Koizumi, Solute segregation in a rapidly solidified Hastelloy-X Ni-based superalloy during laser powder bed fusion investigated by phase-field and computational thermal-fluid dynamics simulations, Addit. Manuf. 84 (2024) 104079, https://doi.org/10.1016/j.addma.2024.104079.

[38] A. Prasad, L. Yuan, P. Lee, M. Patel, D. Qiu, M. Easton, D. StJohn, Towards understanding grain nucleation under Additive Manufacturing solidification conditions, Acta Mater 195 (2020) 392–403, https://doi.org/10.1016/j.actamat.2020.05.012.

[39] T. Ishimoto, N. Morita, R. Ozasa, A. Matsugaki, O. Gokcekaya, S. Higashino, M. Tane, T. Mayama, K. Cho, H.Y. Yasuda, M. Okugawa, Y. Koizumi, M. Yoshiya, D. Egusa, T. Sasaki, E. Abe, H. Kimizuka, N. Ikeo, T. Nakano, Superimpositional design of crystallographic textures and macroscopic shapes via metal additive manufacturing–Game-change in component design, Acta Mater 286 (2025) 120709, https://doi.org/10.1016/j.actamat.2025.120709.

[40] H.-J. Kim, K. Mori, S. Ichikawa, T. Nakano, H. Yamashita, Layered na$_2$ti$_3$o$_7$-supported Ru catalyst for ambient CO$_2$ methanation, Nat. Commun. 16 (2025) 12697, https://doi.org/10.1038/s41467-025-57954-9.

[41] O. Gokcekaya, T. Ishimoto, S. Hibino, J. Yasutomi, T. Narushima, T. Nakano, Unique crystallographic texture formation in Inconel 718 by laser powder bed fusion and its effect on mechanical anisotropy, Acta Mater. 212 (2021) 116876, https://doi.org/10.1016/j.actamat.2021.116876.

[42] Y.M. Wang, T. Voisin, J.T. McKeown, J. Ye, N.P. Calta, Z. Li, Z. Zeng, Y. Zhang, W. Chen, T.T. Roehling, R.T. Ott, M.K. Santala, P.J. Depond, M.J. Matthews, A. V. Hamza, T. Zhu, Additively manufactured hierarchical stainless steels with high strength and ductility, Nat. Mater. 17 (2018) 63–71, https://doi.org/10.1038/nmat5021.

[43] T.G. Gallmeyer, S. Moorthy, B.B. Kappes, M.J. Mills, B. Amin-Ahmadi, A. P. Stebner, Knowledge of process-structure-property relationships to engineer better heat treatments for laser powder bed fusion additive manufactured Inconel 718, Addit. Manuf. 31 (2020) 100977, https://doi.org/10.1016/j.addma.2019.100977.

[44] J. Kwon, G.M. Karthik, Y. Estrin, H.S. Kim, Constitutive modeling of cellular-structured metals produced by additive manufacturing, Acta Mater. 241 (2022) 118421, https://doi.org/10.1016/j.actamat.2022.118421.

[45] T. Mayama, T. Ishimoto, M. Tane, K. Cho, K. Manabe, D. Miyashita, S. Higashino, T. Kikukawa, H.Y. Yasuda, T. Nakano, Novel strengthening mechanism of laser powder bed fusion-manufactured Inconel 718: effects of customized hierarchical interfaces, Addit. Manuf. 93 (2024) 104412, https://doi.org/10.1016/j.addma.2024.104412.

[46] S. Harjo, N. Tsuchida, J. Abe, W. Gong, Martensite phase stress and the strengthening mechanism in TRIP steel by neutron diffraction, Sci. Rep. 7 (2017) 15149, https://doi.org/10.1038/s41598-017-15252-5.

[47] K. Cho, R. Morioka, S. Harjo, T. Kawasaki, H.Y. Yasuda, Study on formation mechanism of {332}<113>deformation twinning in metastable β-type Ti alloy focusing on stress-induced α" martensite phase, Scr. Mater. 177 (2020) 106–111, https://doi.org/10.1016/j.scriptamat.2019.10.011.

[48] R. Oishi, M. Yonemura, Y. Nishimaki, S. Torii, A. Hoshikawa, T. Ishigaki, T. Morishima, K. Mori, T. Kamiyama, Rietveld analysis software for J-PARC, Nucl.

Instrum. Methods A 600 (2009) 94–96, https://doi.org/10.1016/j.nima.2008.11.056.

[49] D. Peirce, R.J. Asaro, A. Needleman, Material rate dependence and localized deformation in crystalline solids, Acta Metall. 31 (1983) 1951–1976, https://doi.org/10.1016/0001-6160(83)90014-7.

[50] Flow Science, Flow-3d, Available online, https://www.flow3d.com/products/flow-3d/, 2025. accessed on 15 April.

[51] C. Tang, J.L. Tan, C.H. Wong, A numerical investigation on the physical mechanisms of single track defects in selective laser melting, Int. J. Heat. Mass Transf. 126 (2018) 957–968, https://doi.org/10.1016/j.ijheatmasstransfer.2018.06.073.

[52] E.A. Brandes, G.B. Brook, Smithells Metals Reference Book, 7th ed., Butterworth-Heinemann, Oxford, 1997.

[53] N. Saunders, Z. Guo, X. Li, A.P. Miodownik, J.-Ph. Schillé, Using JMatPro to model materials properties and behavior, JOM 55 (2003) 60–65, https://doi.org/10.1007/s11837-003-0013-2.

[54] S.-H. Sun, T. Ishimoto, K. Hagihara, Y. Tsutsumi, T. Hanawa, T. Nakano, Excellent mechanical and corrosion properties of austenitic stainless steel with a unique crystallographic lamellar microstructure via selective laser melting, Scr. Mater. 159 (2019) 89–93, https://doi.org/10.1016/j.scriptamat.2018.09.017.

[55] Y.-Q. Wang, W.-W Kong, C. Yuan, Y.-P. Chen, X. Liu, S. Liu, Effects of annealing on microstructures and properties of cold-rolled GH3536 sheet, Mater. Charact. 180 (2021) 111409, https://doi.org/10.1016/j.matchar.2021.111409.

[56] S. Sui, H. Tan, J. Chen, C. Zhong, Z. Li, W. Fan, A. Gasser, W. Huang, The influence of laves phases on the room temperature tensile properties of Inconel 718 fabricated by powder feeding laser additive manufacturing, Acta Mater. 164 (2019) 413–427, https://doi.org/10.1016/j.actamat.2018.10.032.

[57] J.C. Franco-Correa, E. Martínez-Franco, J.M. Alvarado-Orozco, L.A. Cáceres-Díaz, D.G. Espinosa-Arbelaez, J.A. Villada, Effect of conventional heat treatments on the microstructure and microhardness of IN718 obtained by wrought and additive manufacturing, J. Mater. Eng. Perform. 30 (2021) 7035–7045, https://doi.org/10.1007/s11665-021-06138-9.

[58] M. Tane, S. Akita, T. Nakano, K. Hagihara, Y. Umakoshi, M. Niinomi, H. Nakajima, Peculiar elastic behavior of Ti-Nb-Ta-Zr single crystals, Acta Mater. 56 (2008) 2856–2863, https://doi.org/10.1016/j.actamat.2008.02.017.

[59] A. Takase, T. Ishimoto, R. Suganuma, T. Nakano, Lattice distortion in selective laser melting (SLM)-manufactured unstable β-type Ti-15Mo-5Zr-3Al alloy analyzed by high-precision X-ray diffractometry, Scr. Mater. 201 (2021) 113953, https://doi.org/10.1016/j.scriptamat.2021.113953.

[60] P. Pant, S. Proper, V. Luzin, S. Sjöström, K. Simonsson, J. Moverare, S. Hosseini, V. Pacheco, R.L. Peng, Mapping of residual stresses in as-built Inconel 718 fabricated by laser powder bed fusion: a neutron diffraction study of build orientation influence on residual stresses, Addit. Manuf. 55 (2022) 102839, https://doi.org/10.1016/j.addma.2020.101501.

[61] C.L. Johnson, M.J. Hÿtch, P.R. Buseck, Nanoscale waviness of low-angle grain boundaries, PNAS 101 (2004) 17936–17939, https://doi.org/10.1073/pnas.0408348102.

[62] S.-H. Kang, Y. Deguchi, K. Yamamoto, K. Ogi, M. Shirai, Solidification process and behavior of alloying elements in Ni-based superalloy Inconel718, Mater. Trans. 45 (2004) 2728–2733, https://doi.org/10.2320/matertrans.45.2728.

[63] A. Breidi, J.D.T. Allen, A. Mottura, First-principles calculations of intrinsic stacking fault energies and elastic properties in binary nickel alloys, Materialia 35 (2024) 102080, https://doi.org/10.1016/j.mtla.2024.102080.

[64] T.S. Byun, On the stress dependence of partial dislocation separation and deformation microstructure in austenitic stainless steels, Acta Mater. 51 (2003) 3063–3071, https://doi.org/10.1016/S1359-6454(03)00117-4.

[65] E. Rodary, D. Rodney, L. Proville, Y. Bréchet, G. Martin, Dislocation glide in model Ni(Al) solid solutions by molecular dynamics, Phys. Rev. B 70 (2004) 054111, https://doi.org/10.1103/PhysRevB.70.054111.

[66] P.B. Hirsch, A. Kelly, Stacking-fault strengthening, Phil. Mag. 12 (1965) 881–900, https://doi.org/10.1080/14786436508228118.

[67] B. Lane, J. Heigel, R. Ricker, I. Zhirnov, V. Khromschenko, J. Weaver, T. Phan, M. Stoudt, S. Mekhontsev, L. Levine, Measurements of melt pool geometry and cooling rates of individual laser traces on IN625 bare plates, Integr. Mater. Manuf. Innov. 9 (2020) 16–30, https://doi.org/10.1007/s40192-020-00169-1.

[68] J. Lipton, M.E. Glicksman, W. Kurz, Dendritic growth into undercooled alloy metals, Mater. Sci. Eng. 65 (1984) 57–63, https://doi.org/10.1016/0025-5416(84)90199-X.

[69] M.J. Ansari, D.-S. Nguyen, H.S. Park, Investigation of SLM process in terms of temperature distribution and melting pool size: modeling and experimental approaches, Mater. (Basel) 12 (2019) 1272, https://doi.org/10.3390/ma12081272.

[70] C. Keller, E. Hug, Hall–Petch behaviour of Ni polycrystals with a few grains per thickness, Mater. Lett. 62 (2008) 1718–1720, https://doi.org/10.1016/j.matlet.2007.09.069.

[71] J.P. Hirth, J. Lothe, Theory of Dislocations, 2nd Ed., John Wiley and Sons, New York, 1982.

[72] R.W. Armstrong, The yield and flow stress dependence on polycrystal grain size, in: T.N. Baker (Ed.), Yield, Flow and Fracture of Polycrystals, Applied Science Publishers, London, 1983.